



THE UNIVERSITY *of* EDINBURGH

Edinburgh Research Explorer

The exhumation history of the middle Hsuehshan Range, Taiwan, as revealed by zircon thermochronological modeling

Citation for published version:

Shyu, CJ, Tan, E, Kirstein, L, Stuart, F & Chen, Y-G 2023, 'The exhumation history of the middle Hsuehshan Range, Taiwan, as revealed by zircon thermochronological modeling', *Tectonophysics*, vol. 860, 229907. <https://doi.org/10.1016/j.tecto.2023.229907>

Digital Object Identifier (DOI):

[10.1016/j.tecto.2023.229907](https://doi.org/10.1016/j.tecto.2023.229907)

Link:

[Link to publication record in Edinburgh Research Explorer](#)

Document Version:

Peer reviewed version

Published In:

Tectonophysics

General rights

Copyright for the publications made accessible via the Edinburgh Research Explorer is retained by the author(s) and / or other copyright owners and it is a condition of accessing these publications that users recognise and abide by the legal requirements associated with these rights.

Take down policy

The University of Edinburgh has made every reasonable effort to ensure that Edinburgh Research Explorer content complies with UK legislation. If you believe that the public display of this file breaches copyright please contact openaccess@ed.ac.uk providing details, and we will remove access to the work immediately and investigate your claim.



1 **The exhumation history of the middle Hsuehshan Range, Taiwan, as revealed by**
2 **zircon thermochronological modeling**

3
4 **Chase J. Shyu¹, Eh Tan², Linda A. Kirstein³, Finlay M. Stuart⁴, and Yue-Gau Chen^{5,6}**

5 ¹Taiwan International Graduate Program (TIGP) - Earth System Science Program, Academia
6 Sinica and National Central University, Academia Sinica, Taiwan.

7 ²Institute of Earth Sciences, Academia Sinica, Taiwan.

8 ³School of GeoSciences, University of Edinburgh, EH9 3FE, UK.

9 ⁴Scottish Universities Environmental Research Centre, G75 0QF, UK.

10 ⁵Research Center for Environmental Changes, Academia Sinica, Taiwan.

11 ⁶Department of Geosciences, National Taiwan University, Taiwan.

12
13 Corresponding author: Eh Tan (tan2@earth.sinica.edu.tw)

14
15 **Key Points**

- 16 • The ZFT and ZHe ages (5.3 Ma and 2.6 Ma) are the oldest ages recorded in the middle
17 Hsuehshan Range (mid-HR) in Taiwan.
- 18 • The exhumation rate in the mid-HR steadily increases from 0 to 3.4 km/Myr from 6.5
19 to 1 Ma and then increases at a slower rate.
- 20 • A steady increase in the exhumation rate indicates increasing topographic relief, which
21 is likely caused by progressive crustal thickening.

22 **Abstract**

23 The Taiwan orogenic belt has high precipitation and high exhumation rates (3-6 km/Myr),
24 making it a natural laboratory for understanding how erosion, tectonics, and climate interact.
25 Understanding how rock exhumation rates have evolved since the late Miocene is key to
26 unraveling climate–tectonic interactions. In this study, we present 8 new zircon fission track
27 (ZFT) and (U–Th)/He (ZHe) cooling ages (including 2 unreset ages) from 5 samples from

28 1,700 to over 3,300 m elevation around the highly incised Dajia River in the core of the
29 Hsuehshan Range (termed the *mid-HR* in this study) in central Taiwan. Two of the ZFT and
30 ZHe ages (5.3 Ma and 2.6 Ma) are the oldest ages recorded in this region. These ages suggest
31 that the cooling rate of the mid-HR is lower than that of the Backbone Range and Yushan. With
32 these and previously published cooling ages, we modeled the exhumation and cooling history
33 using a 2-D thermal diffusion equation with time-varying erosion. The ZFT and ZHe ages are
34 best explained by a steadily increasing exhumation rate up to $3.4^{+0.5}/_{-0.3}$ km/Myr from 6.5 to
35 1 Ma. The exhumation rate in the last million years is not as well constrained but appears to
36 have increased at a slower rate. Our findings differ from those of previous studies that propose
37 that the exhumation rate increased rapidly in the last 1-2 Myr. We propose that the steady
38 increase in the exhumation rate in the mid-HR indicates increasing topographic relief, which
39 is likely caused by progressive crustal thickening.

40 **1 Introduction**

41 Taiwan is one of the youngest orogens on Earth, resulting from the convergence of the
42 Eurasia continental margin and the Luzon volcanic arc (Ho, 1986; Teng, 1987, 1990) (Fig. 1).
43 It is characterized by several high mountain ranges in the center of Taiwan. The island also
44 receives high precipitation (121-361 cm annually) that is concentrated during the monsoon and
45 typhoon seasons (Yu et al., 2006). The coincidence of high topographic relief and high
46 precipitation means that the region currently experiences some of the highest exhumation rates
47 (3-6 km/Myr) on Earth (Montgomery and Brandon, 2002; Dadson et al., 2003; Galewsky et al.,
48 2006; Derriex et al., 2014) as a result of rock uplift and erosion. The feedback between
49 tectonic uplift, topography, climate, erosion and exhumation is complex and likely nonlinear.
50 The uplift of the Tibetan Plateau and the Andes has nonlinear impacts on the climate and
51 exhumation (Molnar et al., 1993; Braun et al., 2012; Carretier et al., 2013). In the Andes, for
52 instance, the rising mountain range changed the regional precipitation, which in turn affected
53 erosion and exhumation (Barnes et al., 2012; Carretier et al., 2013). Studies have found that
54 exhumation increases nonlinearly after topography reaches the slope or elevation threshold.
55 Similar effects might be present in Taiwan. To understand the process, it is crucial to constrain
56 the history of the uplift/exhumation rates, paleotopography, and paleoclimate. As a first step,
57 we present a detailed determination of the exhumation history, especially how it evolved and
58 when its rate reached the present-day high values.

59 The long-term exhumation rate can be deduced from the rock cooling rates based on
60 low-temperature thermochronometry (LTT). Cooling ages and fission track measurements
61 have been modeled to determine the most likely cooling paths of the Taiwan orogenic belt (Liu,
62 1982; Liu et al., 2000; Willett et al., 2003; Fuller et al., 2006; Lee et al., 2006; Beyssac et al.,
63 2007; Kirstein et al., 2010; Kirstein et al., 2013; Lee et al., 2015; Hsu et al., 2016; Chen et al.,
64 2018; Chen et al., 2019; Huang et al., 2022; Lee et al., 2022).

65 With these data, two distinct tectonic implications are proposed. Willett et al. (2003)
66 and Fuller et al. (2006) utilized numerical thermal models to simulate the cooling processes of
67 the orogenic belt and suggested that the middle latitudes of Taiwan Island have reached a
68 topographic steady state since 2.1-1.5 Ma (Fuller et al., 2006). This implication is consistent
69 with morphological conclusions suggesting that the Taiwan mountain belt has reached a
70 topographic steady state (Suppe, 1981; Barr and Dahlen, 1989; Deffontaines et al., 1994;
71 Willett and Brandon, 2002; Stolar et al., 2007). Several thermochronological studies (Lee et
72 al., 2006; Kirstein et al., 2010; Kirstein et al., 2013; Hsu et al., 2016; Chen et al., 2018) have
73 found evidence of late rapid cooling and proposed the late rapid exhumation hypothesis, where
74 the exhumation rate of Taiwan has rapidly increased in the last 1-2 Myr. This hypothesis was
75 based on the exhumation history that was directly calculated from the cooling rate with the
76 assumption of a constant geothermal gradient, but it was also based on an increased frequency
77 of reset LTT ages (<6 Ma) in sediments younger than 1.9 Ma (Kirstein et al., 2010). As a result,
78 it has been proposed that the uplift mechanism of the Taiwan Orogeny changed at
79 approximately 1-2 Ma (Lee et al., 2006; Kirstein et al., 2010; Hsu et al., 2016; Chen et al.,
80 2018). However, the geothermal gradient in the past is difficult to determine. Brown and
81 Summerfield (1997) indicate that geothermal gradients likely vary significantly with time in
82 tectonically active regions as hot, deep-buried rock is progressively advected to the surface.
83 The late rapid exhumation proposal assumes a constant geothermal gradient and needs to be
84 re-examined. To address the uncertainty in the geothermal gradient, a numerical thermal model
85 is required (Braun et al., 2012; Coutand et al., 2014; McCallister et al., 2014; Fox et al., 2015;
86 Wolff et al., 2020; Dai et al., 2021). Several tools that can obtain an exhumation history from
87 thermochronological data have been developed and are widely used, including Pecube (Braun
88 et al., 2012), Glide (Fox et al., 2014), and age2exhume (van der Beek and Schildgen, 2023).
89 We opted to develop the thermochronological calculation within the thermal–mechanical
90 model *flac* (Cundall, 1989; Tan et al., 2012). We use only the thermal model in this study and

91 plan to incorporate thermal–mechanical deformation with thermochronological modeling in a
92 later study.

93 Taiwan is subdivided into a number of tectono-stratigraphic units from west to east,
94 including the Coastal Plain, the Western Foothills, the Hsuehshan Range (HR), the Backbone
95 Range (BR), the Longitudinal Valley and the Coastal Range. The HR is the second largest
96 mountain range in Taiwan. It lies to the west of the BR. Both mountain ranges are oriented
97 NNE–SSW and formed during the Taiwan Orogeny, which started at approximately 6.5 Ma
98 (Suppe, 1984; Teng, 1992; Liu et al., 2001; Mouthereau et al., 2001; Lin et al., 2003; Kirstein
99 et al., 2010). The earliest rocks that were exhumed during the formation of the BR have been
100 eroded, and only sediment has been preserved in the Coastal Range (Dorsey & Lundberg, 1988).
101 The oldest zircon fission-track (ZFT) ages from the core of the HR are 4.6 Ma (Lee et al., 2015).
102 These ages are significantly younger than the onset of orogenesis, implying that the rocks that
103 were exhumed earlier have been eroded away or have yet to be sampled. The HR has lower
104 cooling and exhumation rates than the BR (Simoes et al., 2007; Derrieux et al., 2014); hence,
105 it is more likely to preserve the record of the early stage of exhumation. Our study area is
106 located in the core of the HR, and it is termed the *mid-HR* in this study.

107 Previously published thermochronological data from the mid-HR were predominantly
108 collected along the Central Cross-Island Highway, which follows river valleys and cuts through
109 several tectonic units (Tsao, 1996; Liu et al., 2001; Fuller et al., 2006; Lee et al., 2006; Lan,
110 2009; Liang, 2011; Lee et al., 2015). Most of these samples represent only limited elevation
111 variation within each unit (1000–1500 m). A few samples from the highest elevations (Lee et
112 al., 2015) have been analyzed with only ZFT. In this paper, we use ZFT and (U–Th)/He (ZHe)
113 thermochronometry of high-elevation samples from the mid-HR to investigate the exhumation
114 history and to test the late rapid exhumation model. The ZFT and ZHe age-elevation profiles
115 are combined with published datasets (e.g., Tsao (1996); Liu et al. (2001); Fuller et al. (2006);
116 Lee et al. (2006); Beyssac et al. (2007); Lan (2009); Liang (2011); Lee et al. (2015)) and a
117 time-dependent 2-D thermal model with erosion to simulate the cooling history. We constrain
118 the exhumation history of the HR and discuss the implications for exhumation.

119 **2 Geological background**

120 Taiwan is located on the boundary between the Philippine Sea Plate and the Eurasia
121 Plate (Fig. 1). The Philippine Sea Plate is moving at ~82 mm/yr in a NW direction with respect
122 to the Eurasian plate (Yu et al., 1997). The HR was a Paleogene half-graben filled with Eocene-

123 to-Oligocene sediments, which were metamorphosed during the Taiwan Orogeny (Teng, 1992,
124 2007). The strata in the HR have undergone deep burial (~10 km) and moderate greenschist-
125 facies metamorphism (300–450°C) (Chen and Wang, 1995; Fuller et al., 2006; Beyssac et al.,
126 2007; Chen et al., 2018). The foreland sandstone consists of clasts sourced from the mid-HR.
127 Chen et al. (2019) analyzed sandstones to constrain when the metamorphic rocks were exposed
128 on the surface and found that the onset of exhumation of the mid-HR likely occurred earlier
129 than 4.3 Ma, which is consistent with the oldest reset ZFT age of 4.6 Ma in this region (Lee et
130 al., 2015). ZFT ages in the central core of the mid-HR are all reset and younger than 6.5 Ma,
131 which indicates that they were cooled during the Taiwan Orogeny. In contrast, ZFT ages from
132 the eastern and western flanks are older (14.6-100 Ma), indicating that they have not been
133 heated above 300°C in the last 14 Myr (Fig. 1). This finding indicates that the central core has
134 experienced the highest exhumation (Fuller et al., 2006; Beyssac et al., 2007). In addition to
135 zircon, apatite is another common mineral for LTT. Unfortunately, apatite grains are rarely
136 contained in the source rock in the mid-HR. Therefore, their ages are not included in this study.

137 No cooling rate has been reported for the mid-HR. In the northern HR, the cooling rate
138 was negligible between 6 and 2.5 Ma, increased to 120°C/Myr between 2.5 and 1.6 Ma and
139 then became 90°C/Myr since 1.6 Ma (Chen et al., 2018). Inverse thermal modeling in the
140 northern BR (to the east of the mid-HR) indicates that the cooling rate was 5-21°C/Myr before
141 2.5 Ma, increased significantly to 75-85°C/Myr between 2.5 and 0.5 Ma and increased further
142 to 460-530°C/Myr in the last 0.5 Myr (Hsu et al., 2016). The cooling history from the adjacent
143 regions suggests that the mid-HR also experienced late rapid cooling in the last 2 Myr.

144 The present-day geothermal gradient of the HR is likely high but spatially varying. The
145 present-day surface heat flow in the HR is derived from thermal wells (Lee and Cheng, 1986;
146 Wu et al., 2013) and silica geothermometry (Liu et al., 2015) is approximately 50-300 mW/m²,
147 which corresponds to a geothermal gradient of 30-90°C/km near the surface. Within the top 10
148 km, the average geothermal gradient, which is inferred from the Curie depth, is approximately
149 50°C/km (Hsieh et al., 2014).

150 The uplift mechanism of the HR has been proposed through three primary concepts:
151 basal accretion and underplating at the decollement (Chapple, 1978; Suppe, 1981; Davis et al.,
152 1983; Barr and Dahlen, 1989; Simoes et al., 2007), the fault-bounded pop-up structure (Clark
153 et al., 1993; Lee et al., 1997), and subvertical elongation (Clark et al., 1993; Tillman and Byrne,
154 1995). The deformation in the mid-HR is mainly due to ductile folding rather than brittle
155 faulting (Liu et al., 2009). The folds are widely distributed and have wavelengths of tens to

156 several thousands of meters (Liu and Kao, 2011). Previous studies have indicated the
157 penetrative coaxial strain history and the subvertical elongation of the HR (Clark et al., 1993;
158 Tillman and Byrne, 1995) Additionally, Kidder et al. (2012) suggest an axial strain of 0.3
159 during deformation at the Kuangmingchiao Anticlinorium (Kmc) (also known as the Dachein
160 Anticline) located at approximately 121.1°E in Fig. 1. The coaxial deformation in the mid-HR
161 makes the Kmc a suitable target for our study.

162 We collected samples along the A-A' profile (Fig. 1), which runs parallel to the Kmc
163 in a NE–SW direction. This profile cuts through the Dajia River valley (Fig. 1) and extends
164 from the riverbed (1000 m elevation) to the mountain peak (3300 m elevation). The profile is
165 7 km long and has a height difference of 2.3 km. We collected three coarse-grained meta-
166 sandstone samples from the Eocene Tachien Formation along the A-A' profile and another two
167 samples from the Paileng Formation in the northwestern region (Fig. 1).

168 **3 Thermochronology**

169 Zircons were separated and picked under a binocular microscope from the 75-350 μm
170 fraction of crushed samples. ZFT dating followed the procedures of Liu et al. (2000) and used
171 the external detector method for sample processing and age calculations. The zeta (ζ) factor
172 (Hurford and Green, 1983) for the standard Fish Canyon Tuff with standard glass NBS-610
173 was determined to be 30 ± 2 Ma (1σ).

174 The ZHe analysis was conducted in the Noble Gas Laboratory at the Scottish
175 Universities Environmental Research Centre. Two to four replicate grains were analyzed for
176 ZHe ages. Each grain was hand-picked, and its dimensions were measured before being loaded
177 into Pt tubes. We followed the procedures of Foeken et al. (2006) for He extraction/analysis
178 and Dobson et al. (2008) for U and Th measurements. The analytical uncertainty in each grain
179 age is 3-5%, mostly due to the uncertainty in the ^4He standard and U and Th spike
180 concentrations (Maino et al., 2019). Correction for He recoil loss was made with established
181 procedures (Hourigan et al., 2005). We assume the uncertainty in grain ages after the correction
182 to be 5%. Age calculations were made following Meesters and Dunai (2005). The uncertainty
183 of the mean age is the standard deviation of the grain ages. If the standard deviation is less than
184 5% of the mean age, we assume the uncertainty to be 5%.

185 The ZFT and ZHe ages of all samples are listed in Table 1. The peak, pooled, and
186 central ZFT ages were calculated and reported for each sample. If the measured
187 thermochronometric age is younger than the onset of the Taiwan Orogeny (6.5 Ma), the grain

188 is considered to be reset. In the following discussion, central ages are used for reset samples.
189 Two ZFT ages (from samples SP01 and ML02) from the Oligocene Paileng Formation in the
190 northwest region are older than 6.5 Ma. These grains have not been reset by the Taiwan
191 Orogeny and are not included in later discussion. The oldest reset ZFT age (5.3 ± 0.5 Ma) is
192 recorded by sample BG02 from the peak of Mt. Baigu (3,189 m), while the youngest age, 3.8
193 ± 0.4 Ma, is recorded by sample DG01 from an elevation of 1,711 m. ZHe ages from these
194 samples range from 2.62 ± 0.13 Ma to 1.94 ± 0.10 Ma (Fig. 2). These new ages from high-
195 elevation samples are older than previously published ZFT cooling ages (Fig. 1) and provide
196 important new constraints on the early exhumation history of the region.

197 A recent development indicates that the ZHe closure temperature could be significantly
198 lower than that calculated by Brandon (2007) due to α -dose damage (Gérard et al., 2022). The
199 work of Gérard et al. (2022) is important for the interpretation of LTT ages, where ZHe, apatite
200 fission track (AFT) and apatite helium ages overlap, specifically where the ZHe ages are
201 younger than the AFT ages. However, there is no evidence of overlapping LTT ages in this
202 region. An AFT age of 0.702 ± 0.28 Ma (Lock, 2007) cited by Chen et al. (2019) is in the river
203 valley of our AER profile. The sample was collected from an elevation of 1286 m. The ZHe
204 ages at a similar location are 1.36 ± 0.10 - 1.51 ± 0.02 Ma (Beysac et al., 2007), with elevations
205 of 1039-1487 m. This finding indicates that the effect of α -dose damage is not important here.

206 The age-elevation relationships (AERs) and previously published data (Table 2) of the
207 A-A' profile are plotted in Fig. 3. A positive correlation between the ZFT and ZHe ages and
208 elevation is clear. We can estimate the apparent exhumation rate from the AERs using two
209 different approaches. First, the slopes of the AERs indicate that the apparent exhumation rates
210 were ~ 1.4 km/Myr from 5 to 2.5 Ma and ~ 1.9 km/Myr from 2.5 to 1.5 Ma, showing a moderate
211 increase in the exhumation rate over time. Second, the apparent exhumation rate can be derived
212 from the apparent cooling rate, which is derived from the difference between the ZHe and ZFT
213 ages. Assuming a constant ZFT closure temperature of 240°C (Hurford, 1986) and a ZHe
214 closure temperature of 180°C (Beysac et al., 2007), the apparent cooling rates can be estimated
215 as $\sim 32^\circ\text{C/Myr}$ at 5.5-2.5 Ma from a high-elevation AER (yellow line above 3000 m in Fig. 3),
216 $\sim 39^\circ\text{C/Myr}$ at 3-1.5 Ma from a low-elevation AER (yellow line below 1000 m in Fig. 3), and
217 $\sim 108^\circ\text{C/Myr}$ from 1.5 Ma to the present day from a low-elevation ZHe (yellow line at
218 approximately 2000 m in Fig. 3). The evolution of the apparent cooling rate is consistent with
219 the previously reported late rapid cooling after ~ 2 Ma in the HR and BR (Lee et al., 2006;
220 Kirstein et al., 2010; Kirstein et al., 2013; Hsu et al., 2016; Chen et al., 2018; Chen et al., 2019).

221 The apparent exhumation rate can be estimated from the age vs. elevation of the same
222 thermochronometer by assuming an unchanged distance between the surface and closure
223 isotherm (i.e., a constant average geothermal gradient). The result (blue line in Fig. 3) is that
224 the apparent exhumation rate was 1.4 km/Myr ($r^2 = 0.71$) during 5-3 Ma and 1.9 km/Myr
225 ($r^2 = 0.95$) during 3-1.5 Ma. The apparent exhumation rate during 1.5-0 Ma can be estimated
226 from the apparent cooling rate by assuming a conventional geothermal gradient. Using
227 25°C/km, the exhumation rate is ~4.3 km/Myr. This again shows a moderate increase during
228 5-1.5 Ma followed by a rapid increase in the last ~2 Myr, which seems to be consistent with
229 the proposal of late rapid exhumation (Lee et al., 2006; Kirstein et al., 2010; Kirstein et al.,
230 2013; Hsu et al., 2016; Chen et al., 2018; Chen et al., 2019). The ZHe samples at low elevations
231 have very similar ages, indicating a high erosion rate around 1.5 Ma.

232 However, the estimates of apparent cooling and exhumation are based on the
233 assumption of constant closure temperatures and geothermal gradients. It is well known that
234 mineral closure temperatures increase when the cooling rate increases (Dodson, 1973, 1979).
235 For example, the closure temperatures of ZFT and ZHe are 232°C and 183°C, respectively,
236 when the cooling rate is 10°C/Myr, and they become 256°C and 207°C, respectively, when the
237 cooling rate is 100°C/Myr (Brandon et al., 1998; Reiners et al., 2004). Additionally, Taiwan is
238 not in a thermal steady state, and its geothermal gradient definitely changes both spatially and
239 temporally. For such a young orogen with high erosion, heat cannot diffuse out sufficiently,
240 leading to a temporal increase in the near-surface geothermal gradient (Brown and
241 Summerfield, 1997). Consequently, the hypothesis of late rapid cooling and exhumation is
242 subject to significant uncertainty. In the following section, we eliminate the assumptions of the
243 constant closure temperature and geothermal gradient by applying a time-dependent thermal
244 model. This model enables us to constrain the evolution of the exhumation rate during the
245 Taiwan Orogeny.

246 **4 Time-dependent thermal models**

247 We modeled the thermal evolution and thermochronometer cooling ages within the A-
248 A' profile with a time-dependent thermal diffusion equation on a 2-D Lagrangian grid. We use
249 *Geoflac for thermochronology* (Shyu et al., 2023), which is based on the *Fast Lagrangian*
250 *Analysis of Continua (FLAC)* algorithm (Cundall, 1989; Tan et al., 2012) and is integrated with
251 thermochronology. The equation of thermal diffusion is solved explicitly as:

252
$$\frac{\partial T}{\partial t} + v_z \frac{\partial T}{\partial z} = \frac{k}{\rho C_p} \frac{\partial^2 T}{\partial z^2}$$

253 where T is the temperature ($^{\circ}\text{C}$), t is time (s), k is the thermal conductivity (3.3 W/m/K),
 254 ρ is the density (2800 kg/m^3), C_p is the specific heat (1000 J/kg/K), and v_z is the imposed uplift
 255 rate (m/s). The top surface has a fixed temperature of 10°C . The other boundaries are thermally
 256 insulating. The top surface is eroded and has a prescribed erosion rate to simulate exhumation.

257 The ZFT and ZHe closure temperatures are cooling-rate dependent (Dodson, 1973,
 258 1979), as calculated by CLOSURE (Brandon et al., 1998; Brandon, 2007). The time of closure
 259 is recorded as the closure age of the thermochronometer.

260 The model domain consists of a 7-km wide and 50-km thick block. The grid spacing is
 261 200 m. The Kmc profile has a 2.4 km elevation change in a 7 km horizontal distance. We
 262 assume that there is no lateral motion within the domain, and we discuss the validity of the
 263 assumption in a later section. With no lateral motion within the profile, the erosion rate at the
 264 surface is identical to the exhumation rate of buried material. We further assume that there is
 265 no differential uplift within the profile since the profile is parallel to the major tectonic lineation
 266 and does not cut across the major tectonic structure. As a result, the height difference within
 267 the profile is produced completely by differential erosion (Fig. 4).

268 The geothermal gradient of the mid-HR at maximum burial was estimated by Raman
 269 spectroscopy of carbonaceous material (RSCM) to be $25\text{-}30^{\circ}\text{C/km}$ (Beyssac et al., 2007). It is
 270 unclear when the temperature gradient reported by RSCM was recorded. The maximum burial
 271 temperature is reported as 450°C , which is within the domain of high-grade greenschist facies.
 272 However, only low-greenschist facies ($\sim 300^{\circ}\text{C}$) has been found in the sediments from the HR
 273 (Yeh, 2017; Chen et al., 2019). Our samples do not show evidence of greenschist-facies
 274 metamorphism, and it is very unlikely that our samples were heated above 300°C . In addition,
 275 if temperatures in the region of 450°C were attained during the Taiwan Orogeny, zircons with
 276 reset ZFTs, whose closure temperature is $\sim 240^{\circ}\text{C}$, should have been exposed much earlier than
 277 1 Ma (Wu, 2018). Therefore, we suspect that the high burial temperature recorded by the
 278 RSCM is likely a prior heating event experienced before the Taiwan Orogeny initiated. With
 279 this uncertainty in mind, we consider the initial geothermal gradient as a model parameter.

280 The HR was initially a sedimentary half-graben. We assume that the initial topography
 281 and isotherms were flat. However, adopting a uniform gradient over the whole depth results in
 282 exceedingly high temperatures and overcooling in the lower half of the model. The geothermal

283 gradient should decrease with depth. We use a half-space cooling model for the initial
 284 temperature and vary its half-space age parameter. Although the half-space cooling model is
 285 valid only for oceanic lithosphere, as it ignores radiogenic heat production and the past thermal
 286 history of the continental lithosphere, it gives a reasonable approximation for the near-surface
 287 temperature profile. The mantle temperature is 1300°C, and the surface temperature is 10°C.
 288 This half-space age parameter is unrelated to the cooling age of thermochronometers but only
 289 a model parameter for the initial temperature. To avoid confusion, we list the corresponding
 290 initial surface geothermal gradient (G_i) within the top 200 m of the half-space cooling model
 291 as the model parameter output.

292 The exhumation is driven by surface erosion. The area that later became Taiwan was a
 293 submarine sedimentary environment (Teng, 1990, 1992). Therefore, we assume that the
 294 erosion rate is 0 km/Myr before the orogeny. We note that the absolute elevation of the surface
 295 has no impact on our thermal model. The model surface has no height difference at the
 296 beginning, but its elevation could be subzero. At the early stage of the collision, the area may
 297 still be submarine and experience submarine erosion. At later stages, the area rises above sea
 298 level and experiences subaerial erosion. Both are included in the erosion in our models. The
 299 erosion rate is 1 km/Myr in the young collision zone in southern Taiwan and increases to ≥ 4
 300 km/Myr in the mature orogen in central Taiwan (Fellin et al., 2017). This suggests that the
 301 erosion rate in Taiwan has increased as the orogen matured. Additionally, the river valley has
 302 a higher erosion rate than the mountain. Hence, the surface erosion rate in our model is
 303 prescribed as a function of both space and time. It can be written as

$$304 \quad \text{erosion rate} = R(t) \left(1 + \Delta R \cos \left(\frac{x}{L} \pi \right) \right)$$

305 where $R(t)$ is the time-dependent spatially averaged erosion rate, ΔR is the amplitude
 306 of differential erosion between the valley and hill, and L is the distance between the valley and
 307 hill (7 km). The prescribed high-erosion region becomes the valley ($x=0$), and the low-erosion
 308 region becomes the peak ($x=L$). The temporal average of $R(t)$ is reported as the temporal
 309 average erosion rate (R_{avg}). We assume that the surface height difference increases with time
 310 and that the rate of increase is proportional to the erosion rate $R(t)$. The proportional constant
 311 ΔR is chosen so that the difference in elevation is 2.4 km (shaded area in Fig. 5a-b) at the end
 312 of the simulation.

313 We consider two scenarios for the evolution of $R(t)$. The first scenario has a constant
 314 erosion rate during the simulation (Fig. 5a). The scenario can be described by two parameters:

315 the temporal average erosion rate, R_{avg} , and the model duration, t_f (6 or 7 Myr), which is the
 316 duration since the onset of exhumation (Liu et al., 2001). We found that the misfits of these
 317 constant models are large, so we have to resort to a more complicated scenario. In the second
 318 scenario, the erosion rate is 0 before the orogeny, gradually increases as the orogeny progresses,
 319 and may further increase, saturate, or decrease at the late stage of the orogeny. Specifically, we
 320 consider the time-varying scenario in two stages (Fig. 5b). At each stage, $R(t)$ is linear. This
 321 scenario has four parameters – the model duration (t_f), $R(t)$ at the end of the second stage (R_f),
 322 duration of the first stage (t_m), and $R(t)/R_f$ at t_m (r_m). The temporal average erosion rate R_{avg} is
 323 affected by these parameters.

324 We vary the initial geothermal gradient (G_t), erosion rate parameters (R_{avg} , r_m , and t_m),
 325 and model duration (t_f) (Table 3). Although the cooling is controlled by erosion and is not
 326 affected by elevation, to match the topography of the A-A' profile (whose average elevation is
 327 2.2 km high) at the end of the model time, a constant uplift rate (v_z) is applied to each model
 328 and is equal to $R_{avg} + 0.367$ km/Myr for $t_f = 6$ Myr or $R_{avg} + 0.315$ km/Myr for $t_f = 7$ Myr.

329 5 Results

330 The model surface is flat at an elevation of 0 km (i.e., no height difference) at the
 331 beginning. The surface height difference increases gradually over time because of differential
 332 erosion. As erosion removes material from the surface, the uplifting rock cools. Exhumation
 333 first occurs in the valley and then at the mountain summit. After a model time of t_f , every model
 334 reaches a height difference of 2.4 km. The closure ages and their elevations at the surface are
 335 then compared to the laboratory AERs in Fig. 3.

336 We evaluate the model AER results by calculating the difference between the model
 337 AER and the laboratory results at the same elevation, weighted by the sample standard
 338 deviation. The misfit (s) of the model result is defined as

$$339 \quad s = \frac{\sum_{i=1}^m \left(\frac{(zhe_{Num} - zhe_i)^2}{\sigma_i^2} \right)}{2m} + \frac{\sum_{j=1}^n \left(\frac{(zft_{Num} - zft_j)^2}{\sigma_j^2} \right)}{2n}$$

340 where m is the number of ZHe ages, n is the number of ZFT ages, zhe_{Num} is the modeled
 341 ZHe age, zft_{Num} is the modeled ZFT age, zhe_i is the i -th ZHe laboratory age, zft_j is the j -th ZFT
 342 laboratory age, σ_i is the standard deviation of the i -th laboratory ZHe age, and σ_j is the standard
 343 deviation of the j -th laboratory ZFT age.

344 We plot the model misfits with respect to the initial thermal gradient G_t and the time-
 345 averaged erosion rate R_{avg} (Fig. 6). If the reset ZHe/ZFT is not exhumed to the surface or only
 346 partially exhumed, the model misfit is colored dark or light gray, respectively, which occurs
 347 when G_t and R_{avg} are both low. Within each series, the trade-off between G_t and R_{avg} is clear.
 348 A model with a high R_{avg} and low G_t has a similar misfit to a model with a low R_{avg} and high
 349 G_t .

350 This scenario is tested by varying r_m , t_m , and t_f in a total of 124 series of models (Fig.
 351 7a, Table 3). We have considered all reasonable variation patterns of the erosion history. For
 352 each series, 572 models with varying R_{avg} and G_t values are explored. The lowest-misfit models
 353 within each of the 124 series are shown in Fig. 7. We classify 124 series of models into 4 types
 354 based on how the erosion rate changes with time and label the representative models (Models
 355 A-D) in each type (Fig. 7b-c, Table 3): constant (Model A), near-steady increase (Model B),
 356 early rapid increase (Model C), and late rapid increase (Model D).

357 **5.1 Representative models of four types**

358 From the representative models of these four types, the models with near-steady
 359 increases (Model B) and early rapid increases (Model C) share the lowest and similar misfits.
 360 These two models have similar G_t and R_{avg} values. Here, we describe Model B (Series 6 in
 361 Table 3) in detail. This is one of the best-fit models (misfit = 1.428), where the erosion rate
 362 increases rapidly from 0 to 1.49 km/Myr from 6 to 5 Ma and then increases less rapidly to 3.73
 363 km/Myr at the present day (Line B in Fig. 7b). The erosion rate reaches 40% of the present-
 364 day value at 5 Ma. The model has values of $R_{avg} = 2.3$ km/Myr, $R_f = 3.73$ km/Myr, and $G_t =$
 365 $17.47^\circ\text{C}/\text{km}$. The material exposed in the valley experiences a rapid change in the local
 366 geothermal gradient during exhumation. The local geothermal gradient is $\sim 17^\circ\text{C}/\text{km}$ at a depth
 367 of ~ 15 km at 6 Ma, $\sim 19^\circ\text{C}/\text{km}$ at a depth of ~ 10 km at 3 Ma, and $\sim 71^\circ\text{C}/\text{km}$ at the surface at
 368 the present day. The average geothermal gradient is $\sim 32^\circ\text{C}/\text{km}$ within the top 10 km depth at
 369 the present day (black line in Fig. 8d). The final surface geothermal gradient is nearly four
 370 times higher than the initial value. The comparison of the model erosion and cooling rate (red
 371 lines in Fig. 7b and 7c) clearly shows that the variations in these rates are not correlated. There
 372 is an ~ 4 Myr time lag between the onset of the distinct increase in the erosion and cooling rates
 373 in the model. For a young orogenic belt, such as Taiwan, this time lag is a significant portion
 374 of the orogen history, which needs to be taken into account when using thermochronometers
 375 to provide insight into orogen evolution. Model C (Series 120 in Table 3) also has a small but

376 slightly higher misfit of 1.532 than Model B. The erosion rate gently decreases in the last 1
 377 Myr (Line C in Fig. 7b). The AERs of this model (green lines in Fig. 7d) are very similar to
 378 those of Model B, demonstrating the nonuniqueness of thermal modeling.

379 Model D (Series 41 in Table 3), with a late rapid increase in the erosion rate, has the
 380 highest misfit of 62.44 among the four representative models. In this model, erosion slowly
 381 increases in the first 4 Myr and rapidly increases in the last 2 Myr (Line D in Fig. 7b). The final
 382 erosion rate is 3.16 km/Myr. The AERs of this model (blue lines in Fig. 7d) have the shallowest
 383 slope among the representative models. However, the age at a low elevation is too young.
 384 Indeed, all late-rapid-increase models have large misfits. This is contradictory to the late rapid
 385 erosion proposed by previous studies in the HR (Hsu et al., 2016; Chen et al., 2018).

386 Model A (Series 1 in Table 3) has a medium misfit of 5.042. The erosion rate is constant
 387 from 6 Ma to the present day (Line A in Fig. 7b). The AERs of Model A (red lines in Fig. 7d)
 388 have steep slopes and small age differences between the ZHe and ZFT AERs. The fit for the
 389 ZHe is satisfactory. However, the ZFT AER is too young and does not match the laboratory
 390 results.

391 **5.2 Ensemble average of low-misfit models**

392 Several models share similar low misfits, demonstrating the nonuniqueness of forward
 393 modeling. We take the ensemble of the top 17 best-fit models (misfits ≤ 1.60 ; Series 6, 7, 17,
 394 18, 33, 64, 74, 85, 86, 99, 109, 110, and 119-123) to calculate the average erosion rate of the
 395 mid-HR (black line in Fig. 7b) and use this ensemble average as our best estimate. Error bars
 396 represent the range of 17 best-fit models at each time. The ensemble average exhumation rate
 397 is $2.2+0.5/-0.4$ km/Myr. The initial average geothermal gradient is $17.1+3.4/-2.6^{\circ}\text{C}/\text{km}$.
 398 Erosion increases steadily from 0 to $3.4+0.5/-0.3$ km/Myr from 7 Ma to 1 Ma. The linear
 399 increase is well constrained. After 1 Ma, the slope of the erosion rate is reduced with larger
 400 uncertainty. We have less confidence in the slowing of the rate increase.

401 We also calculate the ensemble average of the cooling rates of the top 17 best-fit models
 402 (black line in Fig. 7c). The cooling rate increases monotonically and nonlinearly to $121+4.4/-$
 403 $3.6^{\circ}\text{C}/\text{Myr}$ from 7 Ma to 0.5 Ma, followed by a slower increase in the cooling rate with greater
 404 uncertainty at the present day. We find that all cooling histories of the best-fit models (Fig. 7c)
 405 have a similar trend among the 124 model series, regardless of the erosion history. The cooling
 406 rates are low ($<30^{\circ}\text{C}/\text{Myr}$) from 7 to 3 Ma. After 2 Ma, the cooling rates start increasing
 407 significantly and reach approximately $100^{\circ}\text{C}/\text{Myr}$ at 1 Ma. The onset of rapid cooling usually

408 occurs at approximately 2 Ma, despite the variability in the erosion history. When the material
409 is exhumed close to the surface, where the geothermal gradient is high due to earlier erosion,
410 the rock experiences rapid cooling. This is why all thermochronological records in the HR or
411 BR show a rapid increase in the cooling rate from 2 Ma (Lee et al., 2006; Kirstein et al., 2010;
412 Hsu et al., 2016; Chen et al., 2018). The rapid increase in the cooling rate does not necessarily
413 imply an increase in the exhumation/erosion rate, as noted by Mancktelow and Grasemann
414 (1997).

415 **6 Discussion**

416 **6.1 Comparisons to geological observations**

417 Notably, the erosion rates from the model are consistently higher than the apparent rates
418 suggested by the AER. This is because the apparent erosion rate is calculated based on the
419 assumption that the closure depth remains constant over time. However, the geothermal
420 gradient in the HR increases with time. As a result, the closure depth is shallower at the present
421 day than in the past. For example, the ZFT closure depth in Model B migrates upward by ~2
422 km from 5 Ma to 2.5 Ma (red circles in Fig. 8). This upward migration is not considered when
423 calculating the apparent erosion rate. Therefore, it underestimates the true erosion rate. In
424 Model B, the height difference is 2.4 km, while the total exhumation is ~5 km (depth of 13 to
425 7.9 km) in this same time period (brown diamonds in Fig. 8d). This results in an apparent
426 erosion rate of ~1 km/Myr and a true erosion rate of ~2 km/Myr. This difference between
427 apparent and true erosion rates can be estimated only via a forward thermal model.

428 There is evidence of a 1 km/Myr submarine erosion rate south of Taiwan (Das et al.,
429 2021). The study area of Das et al. (2021) has a > 3 km height difference over the nearby sea
430 floor. This indicates that the region is already uplifting, which suggests that this 1 km/Myr
431 erosion rate does not represent the erosion rate at the onset of collision. The erosion rates in
432 Models B and C at 5-6 Ma are ~1 km/Myr. These results suggest that it took approximately 1
433 million years after the onset of collision for the erosion rate to reach 1 km/Myr.

434 We found that the cooling rates in the later stage (< 2 Ma) are consistently much higher
435 than those in the early stage (> 4 Ma) in our models. The ensemble average of the cooling
436 history (black line in Fig. 7c) shows an extremely low cooling rate (<10°C/Myr) from 7 to 4
437 Ma and a low cooling rate (10-20°C/Myr) from 4 to 3 Ma. Then, the cooling rate increases
438 rapidly from 20°C/Myr at 3 Ma to over 130°C/Myr at the present day. This cooling history is
439 generally consistent with multi-thermochronometric data in the northern HR (Chen et al., 2018).

440 Chen et al. (2018) studied the cooling history of a nappe from the northern HR and found that
441 the sample was in a nearly isothermal state until 2.5 Ma, after which the cooling rate increased
442 to 120°C/Myr during 2.5-1.5 Ma and slightly decreased to 90°C/Myr from 1.5 Ma to the present
443 day (green line in Fig. 7c).

444 Model B not only fits the AERs but also satisfies other geological constraints. Model
445 B has an almost linear increase in the maximum burial temperature of exposed samples over
446 time. The exposed maximum burial temperature increases from 100°C at 3 Ma to 210°C at 1
447 Ma and finally to 270°C at the present day (black line in Fig. 9). Model B predicts that very
448 low-grade metamorphic rocks (maximum burial temperature of 200°C) were exhumed to the
449 surface at ~1 Ma, which is supported by petrographic analyses of the sandstone in the Dajia
450 River basin (Yeh, 2017; Chen et al., 2019).

451 The youngest ages are always exposed first at the valley. The reset ZFT in Model B is
452 first exposed at 0.8 Ma with an age of 4.6 Ma and then gradually become younger, with an age
453 of 2.6 Ma at the present day (dashed blue line in Fig. 9). The late exposure of reset ZFT ages
454 is consistent with the observation that reset detrital ZFT ages can be found only within young
455 strata (< 1 Ma) in the Dajia River basin (Wu, 2018). In addition, the reset ZHe in Model B is
456 first exposed at 1.6 Ma with an age of 4 Ma and then gradually become younger, with an age
457 of 1.5 Ma at the present day (solid blue line in Fig. 9). Model B predicts that a reset detrital
458 ZHe value would appear only in strata younger than 1.5 Ma. This prediction awaits future
459 verification.

460 Our thermal simulations can predict the geothermal structures. We take the thermal
461 gradient of the top element layer of the model to calculate the surface geothermal gradient and
462 heat flow. The average surface geothermal gradients and heat flows of the four representative
463 models are as follows: Model A: 39°C/km (128 mW/m²); Model B: 43°C/km (143 mW/m²);
464 Model C: 41°C/km (135 mW/m²); and Model D: 65°C/km (213 mW/m²). The model with a
465 late rapid increase in the erosion rate (Model D) has the highest heat flow, while the model
466 with a constant erosion rate (Model A) has the lowest heat flow. The heat flow of the best-fit
467 model (143 mW/m²) is higher than the observed regional heat flow (100-120 mW/m², Liu et
468 al. (2015)). Then, the average thermal gradient from the top 10 km of the best-fit model (Model
469 B) is 32°C/km, which is lower than the observed regional thermal gradient, as determined by
470 the depth of the Curie point (~50°C/km, Hsieh et al. (2014)). Unfortunately, we cannot
471 reconcile this conflict. Further research is needed.

472 **6.2 Comparison to the model of Simoes et al. (2007)**

473 Simoes et al. (2007) also modeled the thermokinematic evolution of the HR. Here, we
474 compare our model results with theirs. Their exhumation rate is 4.2 km/Myr, starting at 4 Ma,
475 with a total exhumation of 16.8 km. Our ensemble average has a lower average erosion rate
476 ($2.2+0.5/-0.4$ km/Myr), earlier initiation (6-7 Ma), and lower total exhumation (13.2-15.4 km).
477 We attribute the discrepancy to the inclusion of newly reported ZHe and ZFT ages from high
478 elevations and the exclusion of the RSCM temperature (Beysac et al., 2007). Most of the reset
479 ages used in Simoes et al. (2007) were sampled from elevations of 1000-2000 m in the HR.
480 Our high-elevation thermochronological ages are older than the ages used in Simoes et al.
481 (2007), which are less than ~4 Ma (Liu et al., 2001). The older ages push the initiation time of
482 HR exhumation earlier. The lengthened history of the HR decreases the average erosion rate.
483 In addition, the RSCM temperature (Beysac et al., 2007) in the HR is high (~450°C), which
484 suggests a deep burial depth and high exhumation. If the RSCM temperature is included for
485 fitting, we would need to either increase the initial geothermal gradient G_i or the erosion rate.
486 Both changes would reduce the ZHe and ZFT ages, as well as the age difference between them,
487 which would lead to poorer model fits. As discussed in Section 4, we argue that the reported
488 RSCM temperature was likely not acquired during the Taiwan Orogeny but during an earlier
489 heating event. Therefore, the RSCM temperature is excluded from our data.

490 **6.3 Onset of exhumation**

491 We compared two pairs of model series to distinguish the onset of exhumation. The
492 variations in the misfits are opposite between the models. In the pair of models with constant
493 erosion, the misfit of the model with $t_f = 7$ Myr (Series 2 in Table 3) is larger than that of the
494 model with $t_f = 6$ Myr (Series 1). In the pair with linear-increasing erosion, the misfit of the
495 model with $t_f = 7$ Myr (Series 94) is smaller than that of the model with $t_f = 6$ Myr (Series 31).
496 Among the best-fit models (misfit ≤ 1.60), 5 models (Series 6, 7, 17, 18, and 33 in Table 3)
497 have $t_f = 6$ Myr, and 12 models (Series 64, 74, 85, 86, 99, 109, 110, and 119-123) have $t_f = 7$
498 Myr. Therefore, our results cannot distinguish the onset of exhumation in the mid-HR between
499 6 or 7 Myr.

500 **6.4 Implications for Taiwan tectonics**

501 Our results suggest steadily increasing exhumation in the mid-HR. Montgomery and
502 Brandon (2002) reported that the erosion rate increases with the topographic relief of the
503 mountain range. The long-term increase in the erosion rate implies that the large-scale E–W

504 topographic relief in the mid-HR progressively increased during the Taiwan Orogeny. In the
505 last 1 Myr, the erosion rate appears to increase at a slower rate. Fuller et al. (2006) shows that
506 the erosion rate becomes nearly constant once the mountain belt reaches the topographic steady
507 state. This suggests that the mid-HR may be approaching a topographic steady state.

508 The steady increase in the exhumation rate likely resulted from progressively thickened
509 crust. The thickening is recorded by steeply dipping penetrative cleavage (Clark et al., 1993;
510 Tillman and Byrne, 1995). Crustal thickening elevates the topography and increases
511 topographic relief, which in turn increases erosion. We further hypothesize that the progressive
512 crustal thickening is due to constant horizontal shortening from the collision between the
513 Eurasian continental margin and the Luzon arc. If this is true, it has strong implications for the
514 orogenic process in Taiwan.

515 Our newly acquired ZHe ages at high elevations (above 3000 m) in the mid-HR region
516 are approximately twice as old as those in the BR (Lee et al., 2022) and Yushan (Hsu et al.,
517 2016), indicating a significantly lower cooling rate in the mid-HR than in the BR and Yushan.
518 The lower cooling rate of the mid-HR could be attributed to either a lower erosion rate or a
519 deeper closure depth. The long exhumation history of the BR, dating back to 12 Ma (Lo and
520 Yui, 1996; Chen et al., 2019), implies that the geothermal gradient of the BR is higher than that
521 of the mid-HR, resulting in a shallower closure depth and higher cooling rate. However, the
522 comparison of exhumation rates in the BR requires further numerical investigation. For the
523 Yushan region, the similar (Lee et al., 2015) or shorter (Liu et al., 2001) duration of the
524 exhumation history suggests a similar or deeper closure depth but definitely a higher
525 exhumation rate, resulting in a considerably higher cooling rate in the Yushan region.
526 Nonetheless, a further numerical simulation for the Yushan region is still needed to sort out the
527 exhumation histories among the ranges during the Taiwan Orogeny.

528 **6.5 Constraints on erosion rates before 5 Ma and after 1.5 Ma**

529 Our ensemble average has a smaller uncertainty between 1.5 and 5 Ma, where cooling
530 ages are available, and has larger uncertainty before 5 Ma and after 1.5 Ma. It is natural to
531 question how well constrained the erosion rates are before 5 Ma and after 1.5 Ma. To address
532 this question, we compare two models, Models A and A' (Series 1 and 71* in Table 3), with
533 very similar G_t values and erosion histories, except for the erosion rate at 6-7 Ma, to gauge the
534 effect of early erosion. Model A has a constant erosion rate, starting from 6 Ma. Model A' has
535 an earlier onset of erosion at 7 Ma. Its erosion rate starts from 0 and reaches a value similar to

536 that of Model A at 6 Ma (Fig. 7b). Model A' has a 2% lower R_{avg} and G_t but higher total
537 exhumation than Model A. It has slightly younger ZFT ages (pink line in Fig. 7d) and a higher
538 misfit than Model A. The earlier onset of erosion of Model A' increases the near-surface
539 geothermal gradient and results in a younger cooling age. This indicates that erosion before 5
540 Ma would change the later temperature and affect the cooling ages. Similarly, erosion after 1
541 Ma changes the total amount of exhumation. Higher total exhumation would result in younger
542 cooling ages. Therefore, we conclude that the erosion rates before 5 Ma and after 1.5 Ma are
543 constrained by the integrated total exhumation.

544 **6.6 Relative motion in the profile plane**

545 In our thermal models, we assume that the material is uplifted at a uniform velocity for
546 simplicity (Fig. 4). This assumption might not be consistent with the regional tectonics, where
547 relative motion within the profile plane might exist. The relative motion can be decomposed
548 into three components: displacement in the plane, displacement out of the plane, and vertical
549 stretching. The A-A' profile is parallel to the major tectonic lineation, which suggests that
550 displacement in the plane is insignificant. We discuss the importance of the other two
551 components individually, as well as their effects on our results.

552 Some studies (Suppe, 1981; Carena et al., 2002; Huang et al., 2015) indicate that there
553 is a detachment beneath the HR (Hung et al., 1999; Shyu and Sieh, 2005; Yue et al., 2005).
554 Materials pass through the profile plane below the detachment and may be underplated. The
555 thermal effect of this deformation is extra cooling at the detachment. This suggests that the
556 erosion rate in the mid-HR might be underestimated in our model. However, this effect should
557 be small. The major deformation mechanism in the mid-HR is folding with the coaxial strain
558 (Liu and Kao, 2011) rather than shearing, which indicates that the surface strata in the mid-HR
559 are not directly disturbed by the deformation at the detachment. The former detachment or
560 underplated material is still buried and yet to be exhumed.

561 Subvertical elongation does occur in the HR (Clark et al., 1993; Tillman and Byrne,
562 1995). The shortening strain is approximately 0.3 in the HR (Kidder et al., 2012). Conversely,
563 the vertical stretching is approximately $1/(1-0.3)=1.4$ times the original thickness. Stretching
564 affects the thermal structure by homogeneously decreasing the geothermal gradient. Therefore,
565 the initial geothermal gradient of the best-fit model might be underestimated.

566 **6.7 Erosion and climate feedback**

567 Erosional processes can shape the topographic relief of the orogenic belt. The
568 regionally high altitude would impact the local climate, and the precipitation variability could
569 change erosional exhumation (Barnes et al., 2012; Champagnac et al., 2012; Carretier et al.,
570 2013). Unlike the nonlinear increase in the Andes (Barnes et al., 2012; Carretier et al., 2013),
571 we do not observe any sudden change in the erosion rate over time. The erosion history does
572 not show a nonlinear increase during the Taiwan Orogeny.

573 **7 Conclusions**

574 New ZFT and ZHe ages from high elevations in the mid-HR are used to construct AERs
575 with a time-dependent thermal model that incorporates erosion. In general, the ensemble
576 average of lower misfit models has a steady increase in the exhumation rate, while models with
577 a late rapid increase in the exhumation rate have larger misfits. All models demonstrate that
578 the region has experienced rapid cooling since 2 Ma, regardless of the exhumation rate history,
579 which indicates that the observations of rapid cooling in the last 2 Ma do not require enhanced
580 exhumation in the same time span. Our results suggest that the mid-HR has undergone
581 progressive crustal thickening, which progressively increases the topographic relief and
582 erosion rate since the onset of the collision.

583 **Acknowledgments**

584 We would like to thank MOST 110-2116-M-001-005 for funding. We are grateful to
585 Tim Byrne and an anonymous reviewer for their valuable feedback and constructive comments
586 on the study. We thank Tsung-Kwei Liu, Yuan-Hsi Lee, Shao-Yi Huang, and Tzu-Tsen Shen
587 for their technical support. We also thank Timothy Lee, Larry Syu-Heng Lai, and Hsi-An Chen
588 for their assistance in collecting samples in the field.

589 **Data and Software Availability Statement**

590 The dating data and the code for modeling, data cleaning, and analysis in the research are
591 provided with an MIT License. They are available in *Geoflac for thermochronology with*
592 *HR2022* (Shyu et al., 2023).

593 **References**

- 594 Barnes, J.B., Ehlers, T.A., Insel, N., McQuarrie, N., Poulsen, C.J., 2012. Linking orography,
595 climate, and exhumation across the central Andes. *Geology* 40 (12), pp. 1135-1138.
596 doi:10.1130/g33229.1.
- 597 Barr, T.D., Dahlen, F.A., 1989. Brittle frictional mountain building: 2. Thermal structure and
598 heat budget. *Journal of Geophysical Research* 94 (B4), p. 3923.
599 doi:10.1029/JB094iB04p03923.
- 600 Beyssac, O., Simoes, M., Avouac, J.P., Farley, K.A., Chen, Y.-G., Chan, Y.-C., Goffé, B.,
601 2007. Late Cenozoic metamorphic evolution and exhumation of Taiwan. *Tectonics* 26
602 (6), pp. 1-32. doi:10.1029/2006tc002064.
- 603 Brandon, M.T., 2007. Programs for Illustrating Closure, Partial Retention, and the Response
604 of Cooling Ages to Erosion: CLOSURE, AGE2EDOT, AND RESPTIME. Yale
605 University.
- 606 Brandon, M.T., Roden-Tice, M.K., Garver, J.I., 1998. Late Cenozoic exhumation of the
607 Cascadia accretionary wedge in the Olympic Mountains, northwest Washington State.
608 *Geological Society of America Bulletin* 110 (8), pp. 985-1009. doi:10.1130/0016-
609 7606(1998)110<0985:lceotc>2.3.co;2.
- 610 Braun, J., van der Beek, P., Valla, P., Robert, X., Herman, F., Glotzbach, C., Pedersen, V.,
611 Perry, C., Simon-Labric, T., Prigent, C., 2012. Quantifying rates of landscape
612 evolution and tectonic processes by thermochronology and numerical modeling of
613 crustal heat transport using PECUBE. *Tectonophysics* 524-525, pp. 1-28.
614 doi:10.1016/j.tecto.2011.12.035.
- 615 Brown, R.W., Summerfield, M.A., 1997. Some uncertainties in the derivation of rates of
616 denudation from thermochronologic data. *Earth Surface Processes and Landforms* 22,
617 pp. 239-248. doi:10.1002/(SICI)1096-9837(199703)22:3<239::AID-
618 ESP751>3.0.CO;2-B.
- 619 Carena, S., Suppe, J., Kao, H., 2002. Active detachment of Taiwan illuminated by small
620 earthquakes and its control of first-order topography. *Geological Society of America*
621 *Bulletin* 30 (10), pp. 935-938. doi:10.1130/0091-
622 7613(2002)030<0935:ADOTIB>2.0.CO;2.
- 623 Carretier, S., Regard, V., Vassallo, R., Aguilar, G., Martinod, J., Riquelme, R., Pepin, E.,
624 Charrier, R., Hérail, G., Farías, M., Guyot, J.-L., Vargas, G., Lagane, C., 2013. Slope
625 and climate variability control of erosion in the Andes of central Chile. *Geology* 41
626 (2), pp. 195-198. doi:10.1130/g33735.1.
- 627 Champagnac, J.-D., Molnar, P., Sue, C., Herman, F., 2012. Tectonics, climate, and mountain
628 topography. *Journal of Geophysical Research: Solid Earth* 117 (B2), pp. n/a-n/a.
629 doi:10.1029/2011jb008348.
- 630 Chapple, W.M., 1978. Mechanics of thin-skinned fold-and-thrust belts. *GSA Bulletin* 89 (8),
631 pp. 1189-1198. doi:10.1130/0016-7606(1978)89<1189:Motfb>2.0.Co;2.
- 632 Chen, C.-H., Wang, C.-H., 1995. Explanatory notes for the metamorphic facies map of
633 Taiwan. Central Geological Survey, MOEA, Taipei.

- 634 Chen, C.-T., Chan, Y.-C., Lo, C.-H., Malavieille, J., Lu, C.-Y., Tang, J.-T., Lee, Y.-H., 2018.
 635 Basal accretion, a major mechanism for mountain building in Taiwan revealed in rock
 636 thermal history. *Journal of Asian Earth Sciences* 152, pp. 80-90.
 637 doi:10.1016/j.jseaes.2017.11.030.
- 638 Chen, W.-S., Yeh, J.-J., Syu, S.-J., 2019. Late Cenozoic exhumation and erosion of the
 639 Taiwan orogenic belt: New insights from petrographic analysis of foreland basin
 640 sediments and thermochronological dating on the metamorphic orogenic wedge.
 641 *Tectonophysics* 750, pp. 56-69. doi:10.1016/j.tecto.2018.09.003.
- 642 Clark, M.B., Fisher, D.M., Lu, C.-Y., Chen, C.-H., 1993. Kinematic analyses of the
 643 Hsüehshan Range, Taiwan: A large-scale pop-up structure. *Tectonics* 12 (1), pp. 205-
 644 217. doi:10.1029/92TC01711.
- 645 Coutand, I., Whipp, D.M., Grujic, D., Bernet, M., Fellin, M.G., Bookhagen, B., Landry, K.R.,
 646 Ghalley, S.K., Duncan, C., 2014. Geometry and kinematics of the Main Himalayan
 647 Thrust and Neogene crustal exhumation in the Bhutanese Himalaya derived from
 648 inversion of multithermochronologic data. *Journal of Geophysical Research: Solid*
 649 *Earth* 119 (2), pp. 1446-1481. doi:10.1002/2013jb010891.
- 650 Cundall, P.A., 1989. Numerical experiments on localization in frictional materials. *Ingenieur-*
 651 *Archiv* 59, pp. 148-159. doi:10.1007/BF00538368.
- 652 Dadson, S.J., Hovius, N., Chen, H., Dade, W.B., Hsieh, M.-L., Willett, S.D., Hu, J.-C.,
 653 Horng, M.-J., Chen, M.-C., Stark, C.P., Lague, D., Lin, J.-C., 2003. Links between
 654 erosion, runoff variability and seismicity in the Taiwan orogen. *Nature* 426 (6967),
 655 pp. 648-651. doi:10.1038/nature02150.
- 656 Dai, J.G., Fox, M., Han, X., Tremblay, M.M., Xu, S.Y., Shuster, D.L., Liu, B.R., Zhang, J.,
 657 Wang, C.S., 2021. Two Stages of Accelerated Exhumation in the Middle Reach of the
 658 Yarlung River, Southern Tibet Since the Mid-Miocene. *Tectonics* 40 (6).
 659 doi:10.1029/2020tc006618.
- 660 Das, P., Lin, A.T.-S., Chen, M.-P.P., Miramontes, E., Liu, C.-S., Huang, N.-W., Kung, J.,
 661 Hsu, S.-K., Pillutla, R.K., Nayak, K., 2021. Deep-sea submarine erosion by the
 662 Kuroshio Current in the Manila accretionary prism, offshore Southern Taiwan.
 663 *Tectonophysics* 807. doi:10.1016/j.tecto.2021.228813.
- 664 Davis, D., Suppe, J., Dahlen, F.A., 1983. Mechanics of fold-and-thrust belts and accretionary
 665 wedges. *Journal of Geophysical Research* 88 (B2), pp. 1153-1172.
 666 doi:10.1029/JB088iB02p01153.
- 667 Deffontaines, B., Lee, J.-C., Angelier, J., Carvalho, J., Rudant, J.-P., 1994. New geomorphic
 668 data on the active Taiwan orogen: A multisource approach. *Journal of Geophysical*
 669 *Research: Solid Earth* 99 (B10), pp. 20243-20266. doi:10.1029/94jb00733.
- 670 Derrieux, F., Siame, L.L., Bourlès, D.L., Chen, R.-F., Braucher, R., Léanni, L., Lee, J.-C.,
 671 Chu, H.-T., Byrne, T.B., 2014. How fast is the denudation of the Taiwan mountain
 672 belt? Perspectives from in situ cosmogenic ¹⁰Be. *Journal of Asian Earth Sciences* 88,
 673 pp. 230-245. doi:10.1016/j.jseaes.2014.03.012.

- 674 Dobson, K.J., Stuart, F.M., Dempster, T.J., 2008. U and Th zonation in Fish Canyon Tuff
675 zircons: Implications for a zircon (U–Th)/He standard. *Geochimica et Cosmochimica*
676 *Acta* 72 (19), pp. 4745-4755. doi:10.1016/j.gca.2008.07.015.
- 677 Dodson, M.H., 1973. Closure temperature in cooling geochronological and petrological
678 systems. *Contribution to Mineralogy and Petrology* 40, pp. 259-274.
679 doi:10.1007/BF00373790.
- 680 Dodson, M.H., 1979. Theory of Cooling ages, in: Jager, E., Hunziker, J.C. (Eds.), *Lecture in*
681 *Isotope Geology*. Springer-Verlag, New York, pp. 194-206. doi:10.1007/978-3-642-
682 67161-6_14.
- 683 Fellin, M.G., Chen, C.-Y., Willett, S.D., Christl, M., Chen, Y.-G., 2017. Erosion rates across
684 space and timescales from a multi-proxy study of rivers of eastern Taiwan. *Global and*
685 *Planetary Change* 157, pp. 174-193. doi:10.1016/j.gloplacha.2017.07.012.
- 686 Foeken, J.P.T., Stuart, F.M., Dobson, K.J., Persano, C., Vilbert, D., 2006. A diode laser
687 system for heating minerals for (U-Th)/He chronometry. *Geochemistry, Geophysics,*
688 *Geosystems* 7 (4). doi:10.1029/2005gc001190.
- 689 Fox, M., Bodin, T., Shuster, D.L., 2015. Abrupt changes in the rate of Andean Plateau uplift
690 from reversible jump Markov Chain Monte Carlo inversion of river profiles.
691 *Geomorphology* 238, pp. 1-14. doi:10.1016/j.geomorph.2015.02.022.
- 692 Fox, M., Reverman, R., Herman, F., Fellin, M.G., Sternai, P., Willett, S.D., 2014. Rock uplift
693 and erosion rate history of the Bergell intrusion from the inversion of low temperature
694 thermochronometric data. *Geochemistry, Geophysics, Geosystems* 15 (4), pp. 1235-
695 1257. doi:10.1002/2013gc005224.
- 696 Fuller, C.W., Willett, S.D., Fisher, D., Lu, C.Y., 2006. A thermomechanical wedge model of
697 Taiwan constrained by fission-track thermochronometry. *Tectonophysics* 425 (1-4),
698 pp. 1-24. doi:10.1016/j.tecto.2006.05.018.
- 699 Galewsky, J., Stark, C.P., Dadson, S., Wu, C.C., Sobel, A.H., Horng, M.J., 2006. Tropical
700 cyclone triggering of sediment discharge in Taiwan. *Journal of Geophysical Research:*
701 *Earth Surface* 111 (F3). doi:10.1029/2005jf000428.
- 702 Gérard, B., Robert, X., Grujic, D., Gautheron, C., Audin, L., Bernet, M., Balvay, M., 2022.
703 Zircon (U-Th)/He Closure Temperature Lower Than Apatite Thermochronometric
704 Systems: Reconciliation of a Paradox. *Minerals* 12 (2). doi:10.3390/min12020145.
- 705 Ho, C.S., 1986. A synthesis of the geologic evolution of Taiwan. *Tectonophysics* 125 (1), pp.
706 1-16. doi:10.1016/0040-1951(86)90004-1.
- 707 Hourigan, J.K., Reiners, P.W., Brandon, M.T., 2005. U-Th zonation-dependent alpha-
708 ejection in (U-Th)/He chronometry. *Geochimica et Cosmochimica Acta* 69 (13), pp.
709 3349-3365. doi:10.1016/j.gca.2005.01.024.
- 710 Hsieh, H.-H., Chen, C.-H., Lin, P.-Y., Yen, H.-Y., 2014. Curie point depth from spectral
711 analysis of magnetic data in Taiwan. *Journal of Asian Earth Sciences* 90, pp. 26-33.
712 doi:10.1016/j.jseaes.2014.04.007.

- 713 Hsu, W.-H., Byrne, T.B., Ouimet, W., Lee, Y.-H., Chen, Y.-G., Soest, M.v., Hodges, K.,
 714 2016. Pleistocene onset of rapid, punctuated exhumation in the eastern Central Range
 715 of the Taiwan orogenic belt. *Geology* 44 (9), pp. 719-722. doi:10.1130/g37914.1.
- 716 Huang, S.-Y., Lee, Y.-H., Mesalles, L., Horng, C.-S., Lu, H.-Y., Tsai, Y.-L., Wu, Y.-J.,
 717 Chen, F.-Y., Tan, X.-B., 2022. Plio-Pleistocene fluvial dynamics in the pro-foreland
 718 basins of Taiwan: Thermochronological constraints and tectonic implications from the
 719 syn-orogenic deposits. *Tectonophysics* 838. doi:10.1016/j.tecto.2022.229486.
- 720 Huang, T.-Y., Gung, Y., Kuo, B.-Y., Chiao, L.-Y., Chen, Y.-N., 2015. Layered deformation
 721 in the Taiwan orogen. *Science* 349 (6249), pp. 720-723. doi:10.1126/science.aab1879.
- 722 Hung, J.-H., Wiltschko, D.V., Lin, H.-C., Hickman, J.B., Fang, P., Bock, Y., 1999. Structure
 723 and motion of the southwestern Taiwan fold and thrust belt. *Terrestrial Atmospheric
 724 and Oceanic Sciences* 10, pp. 543-568. doi:10.3319/TAO.1999.10.3.543(T).
- 725 Hurford, A.J., 1986. Cooling and uplift patterns in the Lepontine Alps South Central
 726 Switzerland and an age of vertical movement on the Insubric fault line. *Contributions
 727 to Mineralogy and Petrology* 92 (4), pp. 413-427. doi:10.1007/BF00374424.
- 728 Hurford, A.J., Green, P.F., 1983. The zeta age calibration of fission-track dating. *Chemical
 729 Geology* 41 (0), pp. 285-317. doi:10.1016/S0009-2541(83)80026-6.
- 730 Kidder, S., Avouac, J.-P., Chan, Y.-C., 2012. Constraints from rocks in the Taiwan orogen on
 731 crustal stress levels and rheology. *Journal of Geophysical Research* 117 (B9), p. 13.
 732 doi:10.1029/2012jb009303.
- 733 Kirstein, L.A., Carter, A., Chen, Y.-G., 2013. Impacts of arc collision on small orogens: new
 734 insights from the Coastal Range detrital record, Taiwan. *Journal of the Geological
 735 Society* 171 (1), pp. 5-8. doi:10.1144/jgs2013-046.
- 736 Kirstein, L.A., Fellin, M.G., Willett, S.D., Carter, A., Chen, Y.-G., Garver, J.I., Lee, D.-C.,
 737 2010. Pliocene onset of rapid exhumation in Taiwan during arc-continent collision:
 738 new insights from detrital thermochronometry. *Basin Research* 22 (3), pp. 270-285.
 739 doi:10.1111/j.1365-2117.2009.00426.x.
- 740 Lan, C.-H., 2009, Fission track dating of zircon from the middle Hsuehshan Range of
 741 Taiwan, Master Thesis, National Chung Cheng University, 72. Retrieved from
 742 <https://hdl.handle.net/11296/q4s3n6>.
- 743 Lee, C.R., Cheng, W.T., 1986. Preliminary heat flow measurements in Taiwan, paper
 744 presented at Fourth Circum-Pacific Energy and Mineral Resources Conference,
 745 Circum-Pac. Counc. for Energy and Miner. Resour., Singapore, pp. 1-9.
- 746 Lee, J.-C., Angelier, J., Chu, H.-T., 1997. Polyphase history and kinematics of a complex
 747 major fault zone in the northern Taiwan mountain belt: the Lishan Fault.
 748 *Tectonophysics* 274 (1–3), pp. 97-115. doi:10.1016/S0040-1951(96)00300-9.
- 749 Lee, Y.-H., Byrne, T.B., Lo, W., Wang, S.-J., Tsao, S.-J., Chen, C.-H., Yu, H.-C., Tan, X.,
 750 van Soest, M., Hodges, K., Mesalles, L., Robinson, H., Fosdick, J.C., 2022. Out of
 751 sequence faulting in the backbone range, Taiwan: Implications for thickening and

- 752 exhumation processes. *Earth and Planetary Science Letters* 594.
 753 doi:10.1016/j.epsl.2022.117711.
- 754 Lee, Y.-H., Chen, C.-C., Liu, T.-K., Ho, H.-C., Lu, H.-Y., Lo, W., 2006. Mountain building
 755 mechanisms in the Southern Central Range of the Taiwan Orogenic Belt — From
 756 accretionary wedge deformation to arc–continental collision. *Earth and Planetary
 757 Science Letters* 252 (3-4), pp. 413-422. doi:10.1016/j.epsl.2006.09.047.
- 758 Lee, Y.H., Byrne, T., Wang, W.H., Lo, W., Rau, R.J., Lu, H.Y., 2015. Simultaneous
 759 mountain building in the Taiwan orogenic belt. *Geology* 43 (5), pp. 451-454.
 760 doi:10.1130/g36373.1.
- 761 Liang, J.-H., 2011, Zircon and apatite fission track dating along the "Lishan fault" and its
 762 tectonic implication, Master Thesis, National Chung Cheng University, 55. Retrieved
 763 from <https://hdl.handle.net/11296/n6auhr>.
- 764 Lin, A.T., Watts, A.B., Hesselbo, S.P., 2003. Cenozoic stratigraphy and subsidence history of
 765 the South China Sea margin in the Taiwan region. *Basin Research* 15 (4), pp. 453-
 766 478. doi:10.1046/j.1365-2117.2003.00215.x.
- 767 Liu, C.-M., Song, S.-R., Kuo, C.-H., 2015. Silica Geothermometry Applications in the
 768 Taiwan Orogenic Belt. *Terrestrial, Atmospheric and Oceanic Sciences* 26 (4).
 769 doi:10.3319/tao.2015.02.09.01(tt).
- 770 Liu, H.-C., Kao, M.-C., 2011. Geological map of Taiwan scale 1:50,000: Lishan. Central
 771 Geological Survey, MOEA, Taipei.
- 772 Liu, H.-C., Lin, C.-W., Yang, C.-N., 2009. On the Stratigraphy and Geological Structures in
 773 Upper Reaches of the Ta-anchi River, Central Taiwan. *Bulletin of the Central
 774 Geological Survey* 22, pp. 29-61.
- 775 Liu, T.-K., 1982. Tectonic implication of fission track ages from the Central Range, Taiwan,
 776 *Proc. Geol. Soc. China*, pp. 22-37.
- 777 Liu, T.-K., Chen, Y.-G., Chen, W.-S., Jiang, S.-H., 2000. Rates of cooling and denudation of
 778 the Early Penglai Orogeny, Taiwan, as assessed by fission-track constraints.
 779 *Tectonophysics* 320, pp. 69-82. doi:10.1016/S0040-1951(00)00028-7.
- 780 Liu, T.-K., Hsieh, S., Chen, Y.-G., Chen, W.-S., 2001. Thermo-kinematic evolution of the
 781 Taiwan oblique-collision mountain belt as revealed by zircon fission track dating.
 782 *Earth and Planetary Science Letters* 186, pp. 45-56. doi:10.1016/S0012-
 783 821X(01)00232-1.
- 784 Lo, C.H., Yui, T.F.U., 1996. $^{40}\text{Ar}/^{39}\text{Ar}$ dating of high-pressure rocks in the tananao
 785 basement complex, Taiwan. *J. Geol. Soc. China* 39 (1), pp. 13-30.
- 786 Lock, J., 2007, Interpreting low-temperature thermochronometric data in fold-and-thrust
 787 belts: An example from the Western Foothills, Taiwan, Ph.D. Thesis, University of
 788 Washington, 204. Retrieved from
 789 [http://gateway.proquest.com/openurl?url_ver=Z39.88-
 790 2004&rft_val_fmt=info:ofi/fmt:kev:mtx:dissertation&res_dat=xri:pqdiss&rft_dat=xri:
 791 pqdiss:3290562.](http://gateway.proquest.com/openurl?url_ver=Z39.88-2004&rft_val_fmt=info:ofi/fmt:kev:mtx:dissertation&res_dat=xri:pqdiss&rft_dat=xri:pqdiss:3290562)

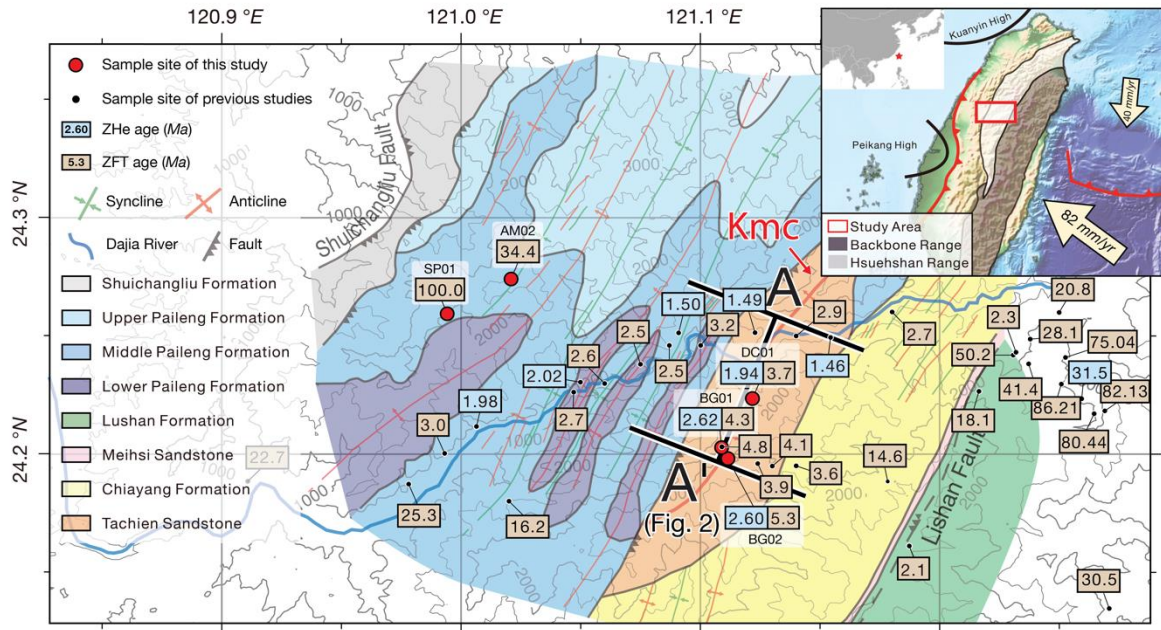
- 792 Maino, M., Gaggero, L., Langone, A., Seno, S., Fanning, M., 2019. Cambro-Silurian
793 magmatisms at the northern Gondwana margin (Penninic basement of the Ligurian
794 Alps). *Geoscience Frontiers* 10 (1), pp. 315-330. doi:10.1016/j.gsf.2018.01.003.
- 795 Mancktelow, N.S., Grasemann, B., 1997. Time-dependent effects of heat advection and
796 topography on cooling histories during erosion. *Tectonophysics* 270 (3–4), pp. 167-
797 195. doi:10.1016/S0040-1951(96)00279-X.
- 798 McCallister, A.T., Taylor, M.H., Murphy, M.A., Styron, R.H., Stockli, D.F., 2014.
799 Thermochronologic constraints on the late Cenozoic exhumation history of the Gurla
800 Mandhata metamorphic core complex, Southwestern Tibet. *Tectonics* 33 (2), pp. 27-
801 52. doi:10.1002/2013tc003302.
- 802 Meesters, A.G.C.A., Dunai, T.J., 2005. A noniterative solution of the (U-Th)/He age
803 equation. *Geochemistry, Geophysics, Geosystems* 6 (4). doi:10.1029/2004gc000834.
- 804 Molnar, P., England, P., Martinod, J., 1993. Mantle dynamics, uplift of the Tibetan Plateau,
805 and the Indian Monsoon. *Reviews of Geophysics* 31 (4), pp. 357-396.
806 doi:10.1029/93RG02030.
- 807 Montgomery, D.R., Brandon, M.T., 2002. Topographic controls on erosion rates in
808 tectonically active mountain ranges. *Earth and Planetary Science Letters* 201 (3), pp.
809 481-489. doi:10.1016/S0012-821X(02)00725-2.
- 810 Mouthereau, F., Lacombe, O., Deffontaines, B., Angelier, J., Brusset, S., 2001. Deformation
811 history of the southwestern Taiwan foreland thrust belt: insights from tectono-
812 sedimentary analyses and balanced cross-sections. *Tectonophysics* 333.
813 doi:10.1016/S0040-1951(00)00280-8.
- 814 Reiners, P.W., Spell, T.L., Nicolescu, S., Zanetti, K.A., 2004. Zircon (U-Th)/He
815 thermochronometry: He diffusion and comparisons with $^{40}\text{Ar}/^{39}\text{Ar}$ dating.
816 *Geochimica et Cosmochimica Acta* 68 (8), pp. 1857-1887.
817 doi:10.1016/j.gca.2003.10.021.
- 818 Shyu, C.J., Tan, E., Lavier, L.L., 2023. Geoflac for thermochronology with HR2022 (Version
819 1.0.3). Zenodo. doi:10.5281/zenodo.7816507.
- 820 Shyu, J.B.H., Sieh, K., 2005. Neotectonic architecture of Taiwan and its implications for
821 future large earthquakes. *Journal of Geophysical Research* 110 (B8).
822 doi:10.1029/2004jb003251.
- 823 Simoes, M., Avouac, J.P., Beyssac, O., Goffé, B., Farley, K.A., Chen, Y.-G., 2007. Mountain
824 building in Taiwan: A thermokinematic model. *Journal of Geophysical Research* 112
825 (B11), p. 25. doi:10.1029/2006jb004824.
- 826 Stolar, D.B., Willett, S.D., Montgomery, D.R., 2007. Characterization of topographic steady
827 state in Taiwan. *Earth and Planetary Science Letters* 261 (3-4), pp. 421-431.
828 doi:10.1016/j.epsl.2007.07.045.
- 829 Suppe, J., 1981. Mechanics of mountain building and metamorphism in Taiwan. *Memoir of*
830 *the Geological Society of China* (4), pp. 67-89.

- 831 Suppe, J., 1984. Kinematics of Arc-Continent Collision, Flipping of Subduction, and Back-
 832 Arc Spreading Near Taiwan. *Memoir of the Geological Society of China* (6), pp. 21-
 833 33.
- 834 Tan, E., Lavier, L.L., Van Avendonk, H.J.A., Heuret, A., 2012. The role of frictional strength
 835 on plate coupling at the subduction interface. *Geochemistry, Geophysics, Geosystems*
 836 13 (10), p. 19. doi:10.1029/2012gc004214.
- 837 Teng, L.S., 1987. Stratigraphic records of the late Cenozoic Penglai orogeny of Taiwan. *Acta*
 838 *Geologica Taiwanica* (25), pp. 205-224.
- 839 Teng, L.S., 1990. Geotectonic evolution of late Cenozoic arc-continent collision in Taiwan.
 840 *Tectonophysics* 183 (1–4), pp. 57-76. doi:10.1016/0040-1951(90)90188-E.
- 841 Teng, L.S., 1992. Geotectonic Evolution of Tertiary Continental Margin Basins of Taiwan.
 842 *Petroleum Geology of Taiwan* 27, pp. 1-19.
- 843 Teng, L.S., 2007. Quaternary Tectonics of Taiwan. Special Publication of the Central
 844 Geological Survey 18, pp. 1-24.
- 845 Tillman, K.S., Byrne, T.B., 1995. Kinematic analysis of the Taiwan Slate Belt. *Tectonics* 14
 846 (2), pp. 322-341. doi:10.1029/94tc02451.
- 847 Tsao, S., 1996, The geological significances of illite crystallinity, zircon fission-track ages,
 848 and K-Ar ages of metasedimentary rocks of the Central Range of Taiwan, Ph.D.
 849 Thesis, National Taiwan University, 272. Retrieved from
 850 <https://hdl.handle.net/11296/aykz26>.
- 851 van der Beek, P., Schildgen, T.F., 2023. Short communication: age2exhume – a
 852 MATLAB/Python script to calculate steady-state vertical exhumation rates from
 853 thermochronometric ages and application to the Himalaya. *Geochronology* 5 (1), pp.
 854 35-49. doi:10.5194/gchron-5-35-2023.
- 855 Willett, S.D., Brandon, M.T., 2002. On steady states in mountain belts. *GSA*.
 856 doi:10.1130/0091-7613(2002)030<0175:OSSIMB>2.0.CO;2.
- 857 Willett, S.D., Fisher, D., Fuller, C., Yeh, E.-C., Lu, C.-Y., 2003. Erosion rates and orogenic-
 858 wedge kinematics in Taiwan inferred from fission-track thermochronometry. *Geology*
 859 31 (11), pp. 945-948. doi:10.1130/G19702.1.
- 860 Wolff, R., Hetzel, R., Dunkl, I., Anczkiewicz, A.A., Pomella, H., 2020. Fast cooling of
 861 normal-fault footwalls: Rapid fault slip or thermal relaxation? *Geology* 48 (4), pp.
 862 333-337. doi:10.1130/g46940.1.
- 863 Wu, S.-K., Chi, W.-C., Hsu, S.-M., Ke, C.-C., Wang, Y., 2013. Shallow crustal thermal
 864 structures of central Taiwan foothills region. *Terr. Atmos. Ocean. Sci.* 24 (4), pp. 695-
 865 707. doi:10.3319/TAO.2013.03.13.01(T).
- 866 Wu, Y.-J., 2018, Detrital Zircon Fission-Track and U-Pb Dating of the Toukoshan and
 867 Cholan Formations in Central Taiwan and its Tectonic Implications, Master Thesis,
 868 National Chung Cheng University, 77. Retrieved from
 869 <https://hdl.handle.net/11296/w4mg2h>.

- 870 Yeh, J.-J., 2017, Petrographic study of the Miocene-Pleistocene sandstone in the Western
871 Foothills, northern Taiwan: implication for the unroofing history of Taiwan orogenic
872 belt, Master Thesis, National Taiwan University, 116. doi:10.6342/NTU201703422.
- 873 Yu, P.-S., Yang, T.-C., Kuo, C.-C., 2006. Evaluating Long-Term Trends in Annual and
874 Seasonal Precipitation in Taiwan. *Water Resources Management* 20 (6), pp. 1007-
875 1023. doi:10.1007/s11269-006-9020-8.
- 876 Yu, S.-B., Chen, H.-Y., Kuo, L.-C., 1997. Velocity field of GPS stations in the Taiwan area.
877 *Tectonophysics* 274, pp. 41-59. doi:10.1016/S0040-1951(96)00297-1.
- 878 Yue, L.-F., Suppe, J., Hung, J.-H., 2005. Structural geology of a classic thrust belt
879 earthquake: the 1999 Chi-Chi earthquake Taiwan (Mw=7.6). *Journal of Structural*
880 *Geology* 27 (11), pp. 2058-2083. doi:10.1016/j.jsg.2005.05.020.

881

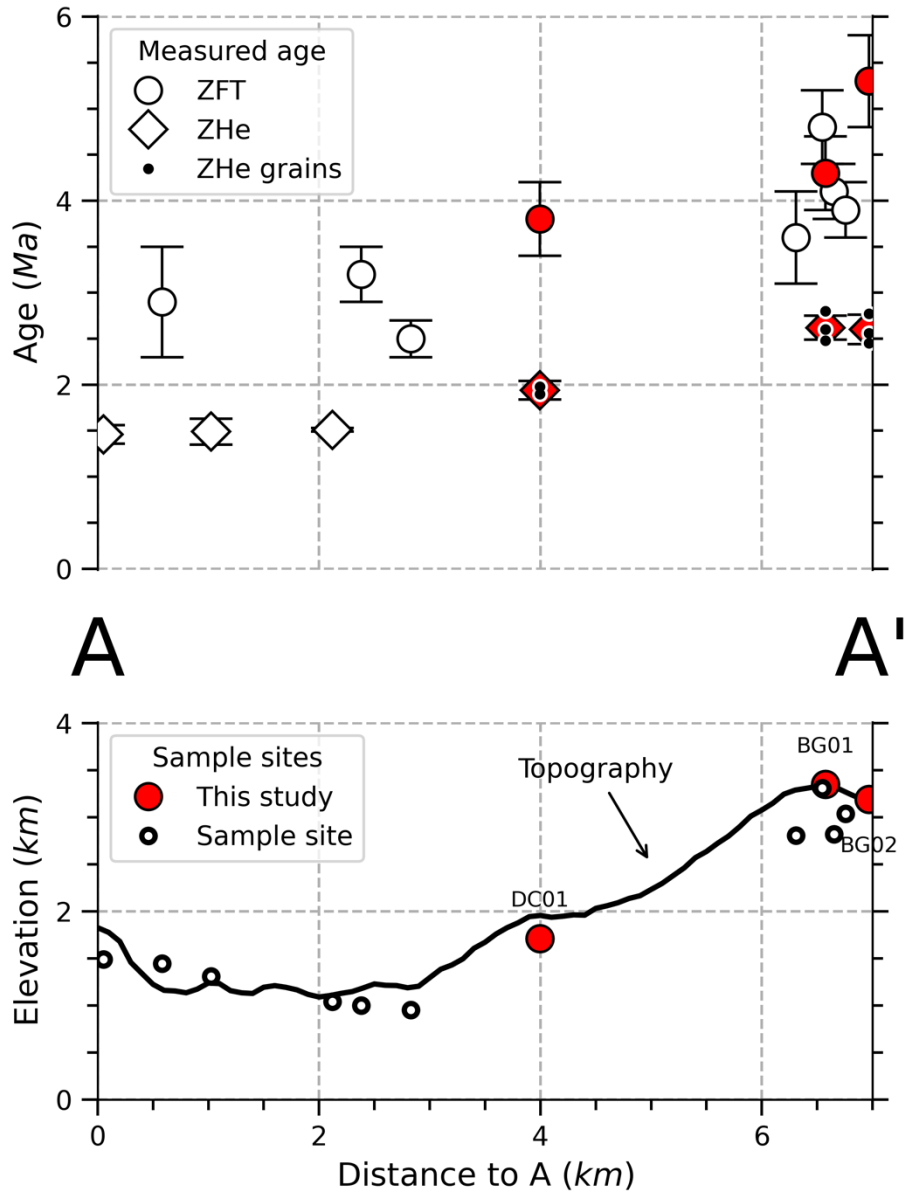
882



883

884 **Figure 1.** Geological formations and structural framework (Liu and Kao, 2010) of the study
 885 area. The inset shows the location of Taiwan and the study area (red rectangle) in the mid-HR
 886 range. The A-A' profile is located along the Kuangmingchiao (Kmc) Anticlinorium. The
 887 cooling ages from this study (red circles) are shown along with data from previous studies
 888 (Tsao, 1996; Liu et al., 2001; Fuller et al., 2006; Lee et al., 2006; Beyssac et al., 2007; Lan,
 889 2009; Liang, 2011; Lee et al., 2015).

890

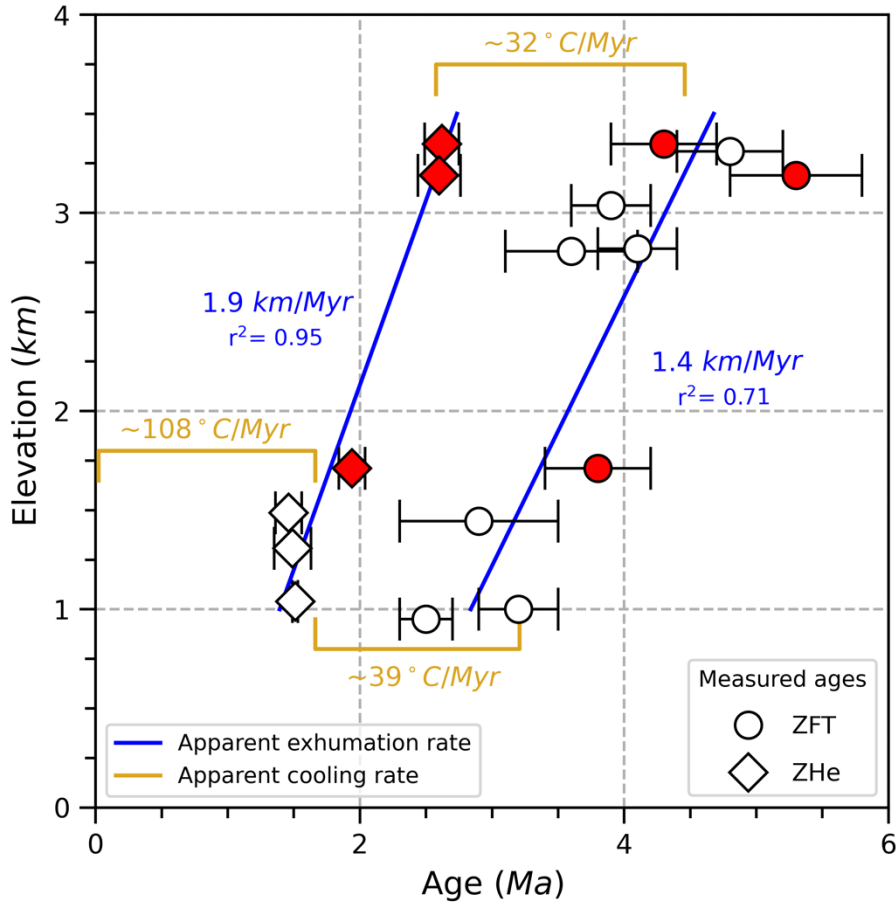


891

892 **Figure 2.** Cooling ages (upper panel) and topography (lower panel) along the A-A' profile are
 893 shown in Figure 1. The three high-elevation samples (red circles) were dated by the ZFT and
 894 ZHe methods in this study (Table 1). Ten samples (open circles) from previous studies (Table
 895 2) are shown.

896

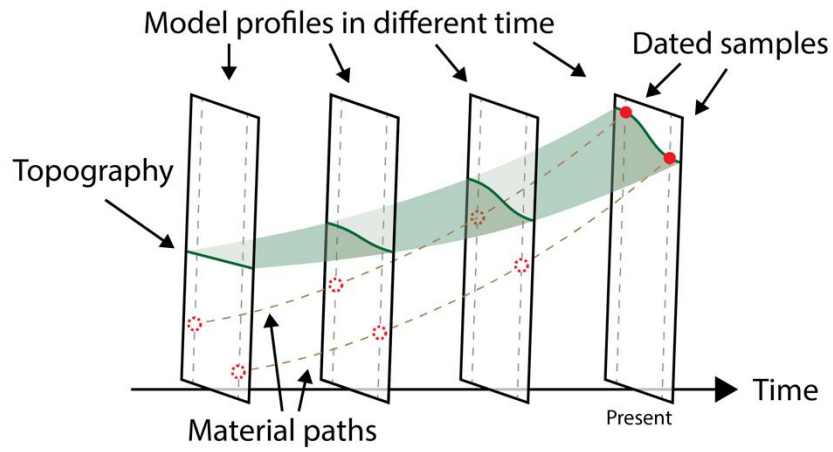
897



898

899 **Figure 3.** ZFT and ZHe cooling ages vs. elevation of samples from along the A-A' profile.
 900 Red symbols are from this study, and open symbols are from previous studies (Table 2). The
 901 linear regressions (blue lines) of the data show the apparent exhumation rates. The temporal
 902 change in the cooling rate is indicated in yellow.

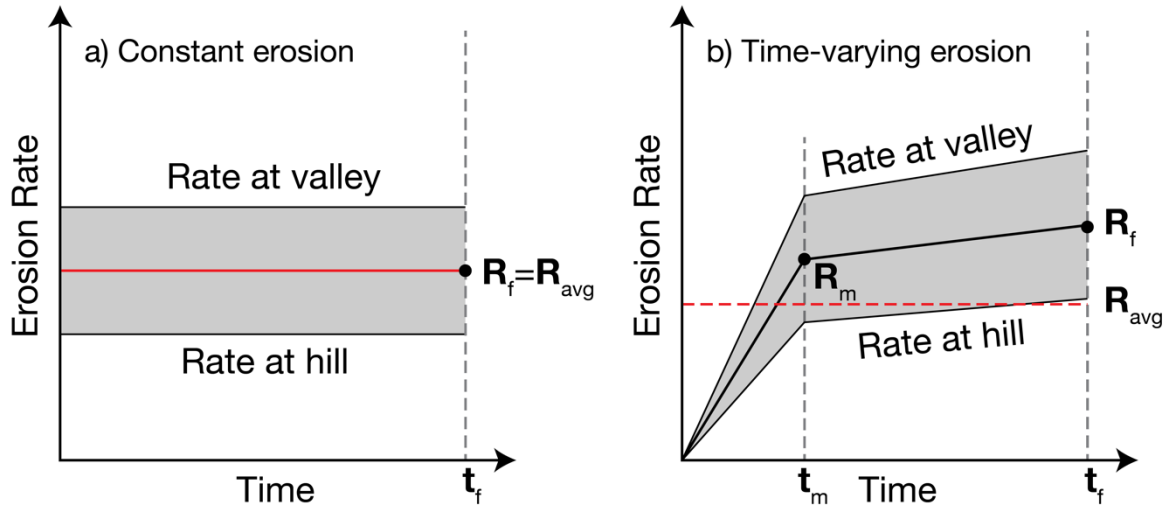
903



904

905 **Figure 4.** Schematic diagram of exhumation in the 2D thermal models. The tectonic uplift
906 elevates the rock while the surface is eroded, which exhumes the rock to the surface.

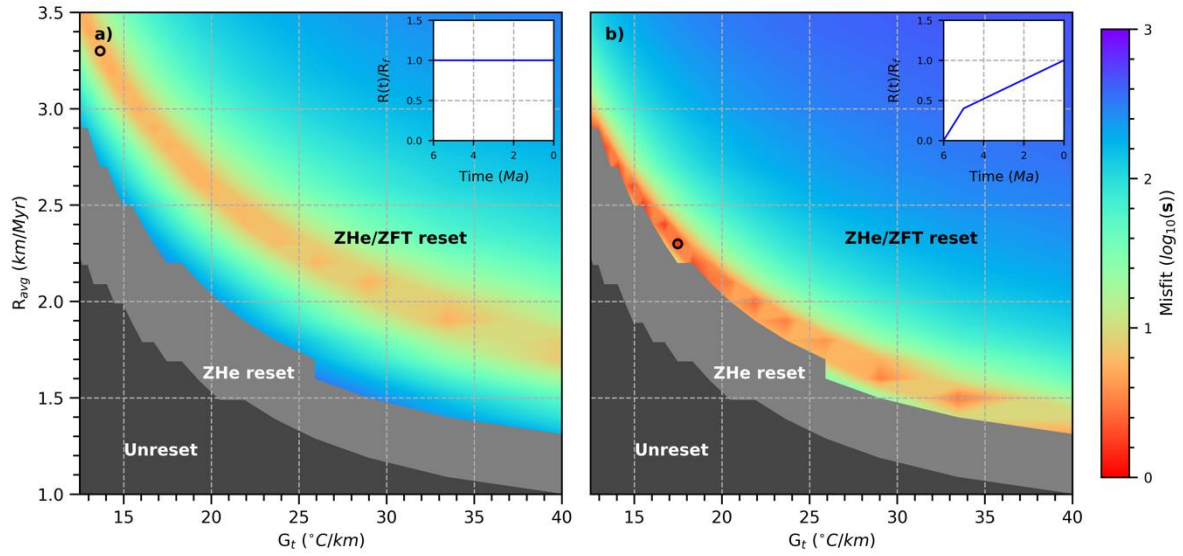
907



908

909 **Figure 5.** Two evolution scenarios, where a) the erosion rate stays constant and b) the erosion
 910 rate has a time-varying increase (or decrease). The thick black lines are the spatially averaged
 911 erosion rates, $R(t)$. The thin black lines above and below are the erosion rates at the valley and
 912 hill, respectively. t_m is the duration of the first stage, and t_f is the duration of the simulation (6
 913 or 7 Myr). R_f is the value of $R(t)$ at the end of the simulation. R_m is the value of $R(t)$
 914 at t_m . $r_m = R_m/R_f$ is the ratio between the rates at the end of the first stage and the second stage. R_{avg} is
 915 the time-averaged erosion rate. The integration over the shaded area is the topographic relief
 916 between the valley and hill.

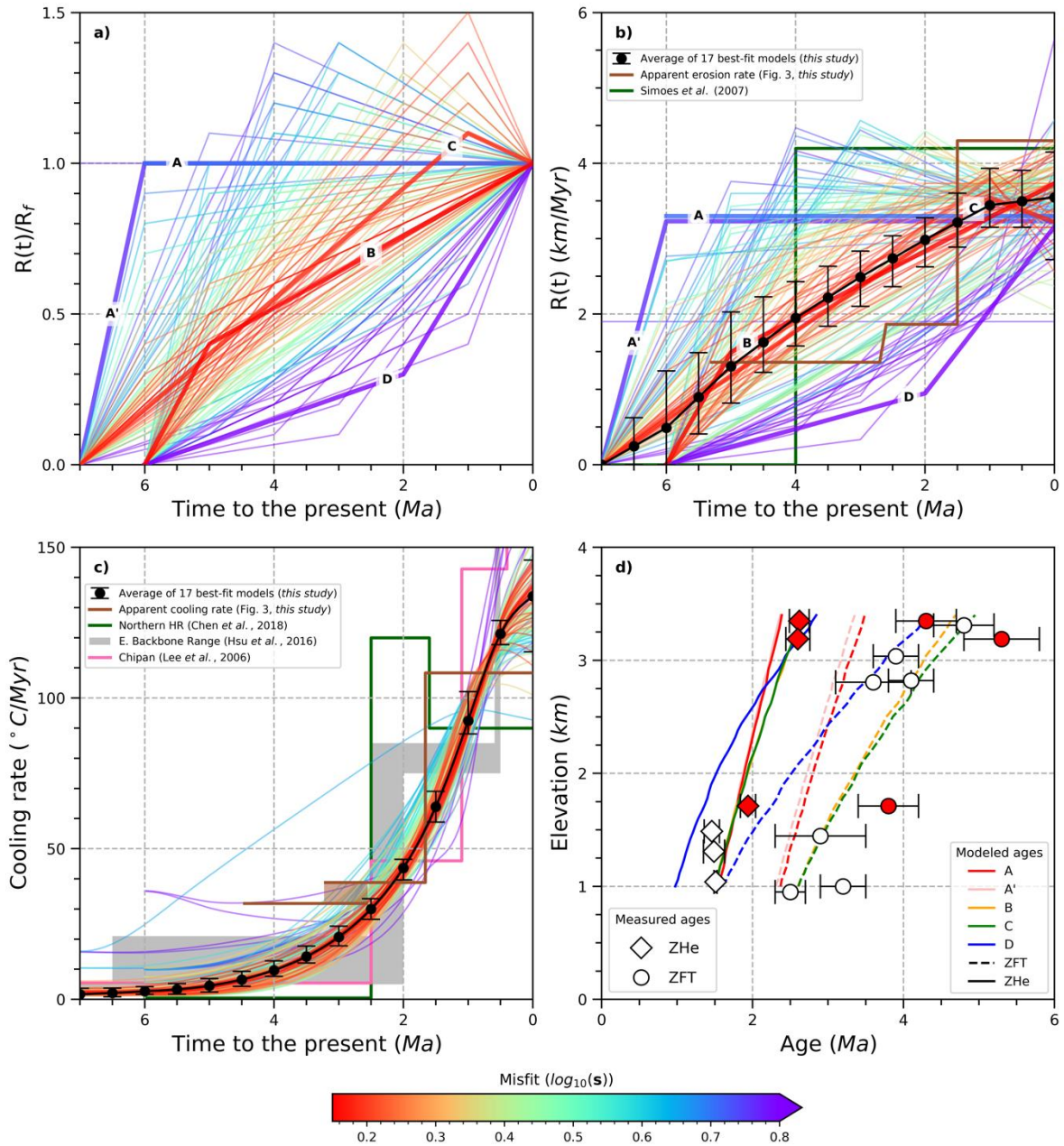
917



918

919 **Figure 6.** Misfits of the a) constant-erosion scenario (Series 1 in Table 3) and b) best-fit series
 920 in the time-varying scenario (Series 6 in Table 3). Within each series, the initial geothermal
 921 gradient (G_t) and the time-averaged erosion rate (R_{avg}) are varied. Black circles are the
 922 minimum misfit of each series. Dark gray indicates the models with unreset ZHe and ZFT
 923 values at the surface. Light gray indicates the models with unreset ZHe values at the surface.
 924 Insets are the relative erosion rate history of each series.

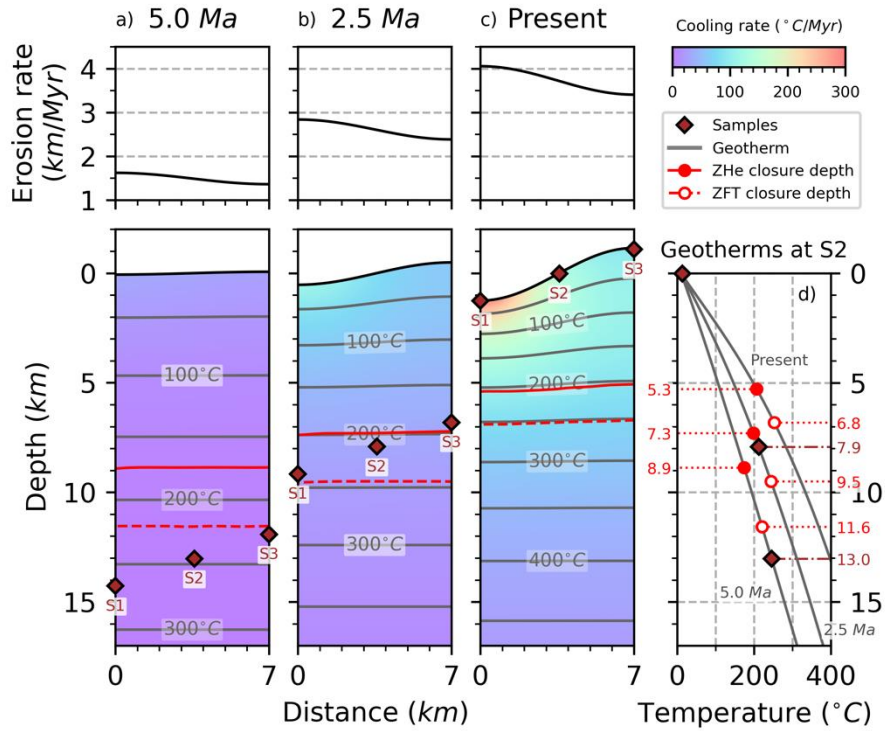
925



926

927 **Figure 7.** Erosion rate, cooling rates, and AER of the model results. a) Relative erosion rate,
 928 $R(t)/R_f$, which is color-coded with model misfits. Labels A-D indicate the four representative
 929 models in the main text. b) Erosion rate, $R(t)$, which is color-coded with misfits and
 930 exhumation/erosion rates estimated by different methods. c) Cooling rate, which is color-coded
 931 with model misfits. d) Modeled AERs of the four representative models. Dashed lines indicate
 932 modeled ZFT ages. Solid lines indicate modeled ZHe ages. Red/open symbols are ages from
 933 this/previous studies. Model A' is used for comparison with Model A, which has similar values
 934 of G_t and a constant erosion rate after 6 Ma but has an earlier onset of erosion rate from 0
 935 km/Myr at 7 Ma. A detailed discussion is provided in Section 6.5.

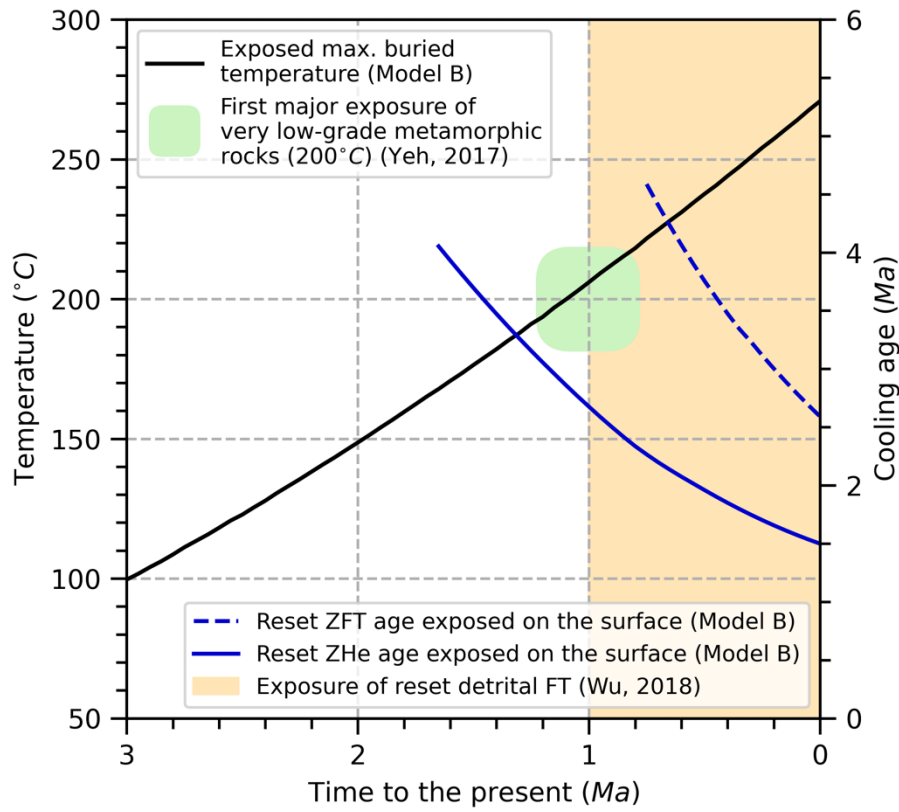
936



937

938 **Figure 8.** Thermal evolution of Model B. The erosion rate, geotherm, cooling rate, and closure
 939 depth at a) 5.0 Ma, b) 2.5 Ma, and c) present. S1-S3 are samples for the model AER. d)
 940 Geothermal profiles at S2 at different times. Numbers indicate the depths of S2 and closure
 941 depths of ZFT and ZHe.

942



943

944 **Figure 9.** The exposure history of reset ZHe/ZFT ages and the maximum burial temperature
 945 in Model B.

946

947

948

949 Table 1. New ZFT and ZHe ages in this study.

ZFT													
Sample	Location		Altitude (m)	Rho_s (cm^{-2})	N_s	Rho_i (cm^{-2})	N_i	Rho_d (cm^{-2})	N_d	Grains	Q	Pooled age ($\pm 1\sigma, Ma$)	Central age ($\pm 1\sigma, Ma$)
	Lon ($^{\circ}E$)	Lat ($^{\circ}N$)											
SP01	120.994	24.259	2093	123.815E+5	1071	20.347E+5	176	11.0E+5	26	10	0.15	99.6 (± 22.2)	100.0 (± 23.2)
AM02	121.021	24.274	2581	58.233E+5	1664	24.217E+5	692	11.0E+5	26	22	0.28	39.6 (± 8.4)	34.4 (± 8.4)
BG01*	121.109	24.203	3348	9.596E+5	730	40.670E+5	3094	12.2E+5	4798	31	0.48	4.3 (± 0.3)	4.3 (± 0.4)
BG02*	121.111	24.198	3189	1.688E+5	774	5.850E+5	2683	12.2E+5	4798	28	0.73	5.3 (± 0.4)	5.3 (± 0.5)
DC01*	121.122	24.223	1711	6.190E+5	462	34.203E+5	2259	12.2E+5	4798	17	0.52	3.7 (± 0.3)	3.8 (± 0.4)

ZHe												
sample	Rep.	Dimensions			Radius (μm)	Term. (#)	^{238}U (ng)	^{232}Th (ng)	4He (ncm^3)	Ft	Raw Age (Ma)	Corrected Age ($\pm 1\sigma, Ma$)
		X (μm)	Y (μm)	Z (μm)								
BG01	A	220	85	80	92	1	3.474	2.224	0.91	0.72	1.87	2.60 (± 0.13)
	B	200	100	75	100	2	1.073	1.563	0.34	0.75	1.95	2.60 (± 0.13)
	C	190	125	120	113	2	5.317	4.226	1.69	0.79	2.20	2.80 (± 0.14)
	D	210	90	80	95	2	3.318	7.043	1.10	0.73	1.81	2.48 (± 0.12)
	mean											2.62 (± 0.13)
BG02	A	230	100	75	105	2	5.737	4.299	1.52	0.76	1.86	2.45 (± 0.12)
	B	200	80	80	86	1.5	2.244	0.721	0.57	0.70	1.94	2.77 (± 0.14)
	C	200	90	80	93	2	1.278	1.930	0.39	0.73	1.87	2.56 (± 0.13)
	mean											2.60 (± 0.16)
DC01	A	240	140	100	133	1	3.412	3.575	0.84	0.82	1.62	1.98 (± 0.10)
	B	350	240	170	214	2	13.335	5.359	2.99	0.89	1.68	1.90 (± 0.09)
	C ⁺	190	110	100	105	2	0.249	0.273	0.33	0.77	8.55	11.17 (± 0.56)
	mean											1.94 (± 0.10)

950 Location: In the WGS84 system, Rho_s is the density of spontaneous tracks, N_s is the number
 951 of spontaneous tracks, Rho_i is the density of induced tracks, N_i is the number of induced tracks,
 952 Rho_d is the density of dosimeter tracks, N_d is the number of dosimeter tracks, Q is the χ^2
 953 probability, Rep. is the replicate, Term. is the termination, and Ft is the Ft correction.

954 *: These samples are also dated by the ZHe method.

955 ⁺: Grain DC01-C is not used in the later analysis since its age is older than the Taiwan Orogeny.

956

957 Table 2. Additional published ZFT and ZHe ages used in this study.

Sample	Location		Altitude (<i>m</i>)	Age ($\pm 1\sigma$) (<i>Ma</i>)
	Lon ($^{\circ}E$)	Lat ($^{\circ}N$)		
ZHe				
C02-41 [§]	121.154	24.250	1487	1.46 (± 0.10)
C04-03 [§]	121.115	24.253	1308	1.49 (± 0.14)
C04-18 [§]	121.091	24.252	1039	1.51 (± 0.02)
ZFT				
CH-308 [§]	121.132	24.251	1445	2.9 (± 0.5)
Beikou_23 [†]	121.130	24.195	2820	4.1 (± 0.3)
Beikou_24 [†]	121.124	24.196	3037	3.9 (± 0.3)
Beikou_28 [†]	121.140	24.195	2806	3.6 (± 0.5)
Beikou_Mt [†]	121.109	24.203	3310	4.8 (± 0.4)
TC012 [†]	121.104	24.240	1100	2.6 (± 0.2)
TC014 [†]	121.095	24.242	1000	2.8 (± 0.2)

958 [§]: *Beysac et al. (2007)*, [§]: *Liu et al. (2001)*, and [†]: *Lee (2015)*.

959

960 Table 3. Parameters of the thermal models.

Series #	t_m (Myr)	t_f (Myr)	r_m (R_m/R_f)	R_f (km/Myr)	Lowest-misfit model				
					R_f (km/Myr)	ΔR	R_{avg} (km/Myr)	G_t ($^{\circ}C/km$)	s
1(A) ^{§†}	-	6	-	1.00-3.50	3.30	0.0606	3.3	13.66	5.042
2	-	7	-	1.00-3.50	1.90	0.0902	1.9	33.45	5.835
3	1	6	0.1	2.14-7.50	2.79	0.1538	1.3	33.45	4.758
4	1	6	0.2	1.94-6.77	2.90	0.1333	1.5	28.97	2.781
5	1	6	0.3	1.76-6.18	3.53	0.1000	2.0	20.49	1.780
6(B) ^{§†}	1	6	0.4	1.62-5.68	3.73	0.0870	2.3	17.47	1.428
7	1	6	0.5	1.50-5.25	4.05	0.0741	2.7	14.49	1.518
8	1	6	0.6	1.40-4.88	4.19	0.0667	3.0	12.96	1.793
9	1	6	0.7	1.30-4.57	3.91	0.0667	3.0	13.29	2.340
10	1	6	0.8	1.22-4.29	3.92	0.0625	3.2	12.64	2.886
11	1	6	0.9	1.15-4.04	3.81	0.0606	3.3	12.35	3.378
12	1	6	1.0	1.09-3.82	3.60	0.0606	3.3	12.64	4.161
13	2	6	0.1	2.61-9.13	4.17	0.1250	1.6	25.91	43.84
14	2	6	0.2	2.31-8.08	3.00	0.1538	1.3	33.45	8.927
15	2	6	0.3	2.07-7.24	3.31	0.1250	1.6	25.91	4.400
16	2	6	0.4	1.88-6.56	4.12	0.0909	2.2	17.47	3.089
17	2	6	0.5	1.71-6.00	3.60	0.0952	2.1	19.31	1.480
18	2	6	0.6	1.58-5.53	3.63	0.0870	2.3	17.47	1.515
19	2	6	0.7	1.46-5.12	4.10	0.0714	2.8	13.66	1.702
20	2	6	0.8	1.36-4.77	3.95	0.0690	2.9	13.29	2.036
21	2	6	0.9	1.28-4.47	3.70	0.0690	2.9	13.66	2.710
22	2	6	1.0	1.20-4.20	3.48	0.0690	2.9	14.05	3.318
23	2	6	1.1	1.13-3.96	3.40	0.0667	3.0	13.66	3.861
24	2	6	1.2	1.07-3.75	3.43	0.0625	3.2	12.64	4.388
25	2	6	1.3	1.02-3.56	3.36	0.0606	3.3	12.35	4.935
26	2	6	1.4	0.97-3.39	3.19	0.0606	3.3	12.64	5.449
27	3	6	0.1	3.33-11.7	3.33	0.2000	1.0	57.94	96.24
28	3	6	0.2	2.86-10.0	4.57	0.1250	1.6	25.91	63.59
29	3	6	0.3	2.50-8.75	3.25	0.1538	1.3	33.45	16.53
30	3	6	0.4	2.22-7.78	2.89	0.1538	1.3	33.45	5.988s
31	3	6	0.5	2.00-7.00	3.20	0.1250	1.6	25.91	3.203
32	3	6	0.6	1.82-6.36	4.00	0.0909	2.2	17.47	2.694
33	3	6	0.7	1.67-5.83	3.50	0.0952	2.1	19.31	1.534
34	3	6	0.8	1.54-5.38	3.85	0.0800	2.5	15.49	1.649
35	3	6	0.9	1.43-5.00	3.71	0.0769	2.6	14.96	1.830
36	3	6	1.0	1.33-4.67	3.73	0.0714	2.8	13.66	2.036
37	3	6	1.1	1.25-4.38	3.62	0.0690	2.9	13.29	2.478
38	3	6	1.2	1.18-4.12	3.65	0.0645	3.1	12.35	2.962
39	3	6	1.3	1.11-3.89	3.44	0.0645	3.1	12.35	3.585
40	3	6	1.4	1.05-3.68	3.26	0.0645	3.1	12.64	4.084
41(D) [†]	4	6	0.3	3.16-11.1	3.16	0.2000	1.0	57.94	62.44
42	4	6	0.4	2.73-9.55	3.55	0.1538	1.3	33.45	20.77
43	4	6	0.5	2.40-8.40	3.12	0.1538	1.3	33.45	7.984
44	4	6	0.6	2.14-7.50	3.43	0.1250	1.6	25.91	4.126
45	4	6	0.7	1.94-6.77	2.90	0.1333	1.5	28.97	2.837
46	4	6	0.8	1.76-6.18	2.47	0.1429	1.4	33.45	2.505
47	4	6	0.9	1.62-5.68	3.57	0.0909	2.2	17.47	1.914
48	4	6	1.0	1.50-5.25	3.15	0.0952	2.1	19.31	1.630
49	4	6	1.1	1.40-4.88	3.35	0.0833	2.4	16.07	1.755
50	4	6	1.2	1.30-4.57	3.26	0.0800	2.5	15.49	1.969
51	4	6	1.3	1.22-4.29	3.31	0.0741	2.7	14.05	2.100
52	4	6	1.4	1.15-4.04	3.12	0.0741	2.7	14.05	2.218
53	5	6	0.4	3.53-12.4	5.65	0.1250	1.6	25.91	34.76
54	5	6	0.5	3.00-10.5	3.90	0.1538	1.3	33.45	9.553
55	5	6	0.6	2.61-9.13	3.39	0.1538	1.3	33.45	6.027
56	5	6	0.7	2.31-8.08	3.69	0.1250	1.6	25.91	4.687
57	5	6	0.9	1.88-6.56	2.81	0.1333	1.5	28.97	2.737
58	5	6	1.0	1.71-6.00	2.57	0.1333	1.5	28.97	2.539
59	5	6	1.1	1.58-5.53	2.37	0.1333	1.5	28.97	2.686
60	5	6	1.2	1.46-5.12	2.05	0.1429	1.4	33.45	2.465
61	5	6	1.3	1.36-4.77	3.00	0.0909	2.2	17.47	2.551

961 For all series, R_{avg} values are 1.0-3.5 km/Myr, the initial thermal ages are 5-110 Ma, and G_t
 962 values are 12.35-57.84 $^{\circ}C/km$. [§]: The misfits of these series, with varying G_t and R_{avg} values,
 963 are shown in Fig. 6. [†]: The lowest-misfit models of these series are labeled in Fig. 7.

964 Table 3. Parameters of the thermal models (continue)

Series #	t _m (Myr)	t _f (Myr)	r _m (R _m /R _f)	R _f (km/Myr)	Lowest-misfit model				
					R _f (km/Myr)	ΔR	R _{avg} (km/Myr)	G _t (°C/km)	s
62	1	7	0.1	2.09-7.31	3.76	0.0952	1.8	19.31	2.089
63	1	7	0.2	1.89-6.62	3.41	0.0952	1.8	20.49	1.639
64	1	7	0.3	1.73-6.05	4.15	0.0714	2.4	14.49	1.517
65	1	7	0.4	1.59-5.57	4.30	0.0635	2.7	12.64	1.772
66	1	7	0.5	1.47-5.16	4.13	0.0612	2.8	12.64	2.181
67	1	7	0.6	1.37-4.80	3.57	0.0659	2.6	14.49	3.063
68	1	7	0.7	1.28-4.50	3.85	0.0571	3.0	12.35	3.588
69	1	7	0.8	1.21-4.22	3.38	0.0612	2.8	14.05	4.241
70	1	7	0.9	1.14-3.98	3.07	0.0635	2.7	15.49	4.987
71	1	7	1.0	1.08-3.77	3.34	0.0553	3.1	12.96	5.526
71(A)*	1	7	1.0	3.23	3.23	0.0571	3.0	13.66	5.751
72	2	7	0.1	2.46-8.60	2.95	0.1429	1.2	33.45	6.161
73	2	7	0.2	2.19-7.66	3.72	0.1008	1.7	20.49	2.913
74	2	7	0.4	1.79-6.28	3.59	0.0857	2.0	18.32	1.513
75	2	7	0.5	1.65-5.76	3.95	0.0714	2.4	14.49	1.804
76	2	7	0.6	1.52-5.33	3.96	0.0659	2.6	13.66	2.071
77	2	7	0.7	1.41-4.95	3.96	0.0612	2.8	12.64	2.626
78	2	7	0.8	1.32-4.62	3.83	0.0591	2.9	12.35	3.405
79	2	7	0.9	1.24-4.34	3.59	0.0591	2.9	12.96	4.258
80	2	7	1.0	1.17-4.08	3.38	0.0591	2.9	13.29	4.874
81	2	7	1.1	1.10-3.86	3.42	0.0553	3.1	12.35	5.461
82	3	7	0.2	2.59-9.07	2.59	0.1714	1.0	40.97	7.816
83	3	7	0.3	2.30-8.03	3.67	0.1071	1.6	21.90	4.050
84	3	7	0.4	2.06-7.21	3.09	0.1143	1.5	25.91	2.086
85	3	7	0.5	1.87-6.53	4.11	0.0779	2.2	15.49	1.543
86	3	7	0.6	1.71-5.98	3.76	0.0779	2.2	16.07	1.537
87	3	7	0.7	1.57-5.51	4.25	0.0635	2.7	12.35	1.934
88	3	7	0.8	1.46-5.10	3.79	0.0659	2.6	13.66	2.564
89	3	7	0.9	1.36-4.76	3.81	0.0612	2.8	12.64	3.213
90	3	7	1.0	1.27-4.45	4.25	0.0591	2.7	12.35	3.950
91	3	7	1.1	1.20-4.19	3.47	0.0591	2.9	12.64	4.624
92	3	7	1.2	1.13-3.95	3.27	0.0591	2.9	12.96	5.365
93	3	7	1.3	1.07-3.74	3.21	0.0571	3.0	12.64	5.960
94	3.5	7	0.5	2.00-7.00	3.40	0.1008	1.7	21.90	1.708
95	4	7	0.3	2.75-9.61	2.75	0.1714	1.0	40.97	10.37
96	4	7	0.4	2.41-8.45	2.90	0.1429	1.2	33.45	4.617
97	4	7	0.5	2.15-7.54	3.88	0.0952	1.8	19.31	2.758
98	4	7	0.6	1.94-6.81	3.89	0.0857	2.0	17.47	1.704
99	4	7	0.7	1.77-6.20	3.72	0.0816	2.1	16.73	1.538
100	4	7	0.8	1.63-5.70	3.74	0.0745	2.3	14.96	1.938
101	4	7	0.9	1.51-5.27	3.91	0.0659	2.6	12.96	2.166
102	4	7	1.0	1.40-4.90	3.64	0.0659	2.6	13.29	2.729
103	4	7	1.1	1.31-4.58	3.66	0.0612	2.8	12.35	3.380
104	4	7	1.2	1.23-4.30	3.44	0.0612	2.8	12.64	4.133
105	4	7	1.3	1.16-4.05	3.24	0.0612	2.8	12.96	4.999
106	4	7	1.4	1.09-3.83	3.17	0.0591	2.9	12.35	5.312
107	5	7	0.5	2.55-8.91	3.82	0.1143	1.5	23.65	5.310
108	5	7	0.6	2.26-7.90	4.06	0.0952	1.8	19.31	3.328
109	5	7	0.8	1.84-6.45	3.68	0.0857	2.0	17.47	1.487
110	5	7	0.9	1.69-5.90	3.54	0.0816	2.1	16.73	1.603
111	5	7	1.0	1.56-5.44	3.73	0.0714	2.4	14.05	1.757
112	5	7	1.1	1.44-5.05	3.75	0.0659	2.6	12.64	2.157
113	5	7	1.2	1.35-4.71	3.50	0.0659	2.6	12.96	2.304
114	5	7	1.3	1.26-4.41	3.41	0.0635	2.7	12.35	2.723
115	6	7	0.6	2.69-9.42	4.58	0.1008	1.7	20.49	3.359
116	6	7	0.7	2.37-8.31	4.27	0.0952	1.8	19.31	2.389
117	6	7	0.8	2.12-7.42	3.39	0.1071	1.6	23.65	1.957
118	6	7	0.9	1.92-6.71	3.64	0.0902	1.9	18.32	1.776
119	6	7	1.0	1.75-6.12	3.15	0.0952	1.8	20.49	1.558
120(C)†	6	7	1.1	1.61-5.63	3.22	0.0857	2.0	17.47	1.532
121	6	7	1.2	1.49-5.21	3.28	0.0779	2.2	15.49	1.592
122	6	7	1.3	1.39-4.85	2.91	0.0816	2.1	16.73	1.548
123	6	7	1.4	1.30-4.54	2.72	0.0816	2.1	16.73	1.559
124	6	7	1.5	1.22-4.26	2.56	0.0816	2.1	16.73	1.662

965 *: This model in Series 71 (Model A') is for the comparison with Model A, which has the
 966 same G_t and 2% lower R_f than that of Model A.